JOURNAL OF PETROLOGY | VOLUME 51 | NUMBER 5 | PAGES 1053–1085 | 2010 | doi:10.1093/petrology/egq011

Magmatic Longevity of Laacher See Volcano (Eifel, Germany) Indicated by U–Th Dating of Intrusive Carbonatites

AXEL K. SCHMITT[1,*], FLORIAN WETZEL[2,3], KARI M. COOPER[4], HAIBO ZOU[5] AND GERHARD WÖRNER[2]

[1]DEPARTMENT OF EARTH AND SPACE SCIENCES, UNIVERSITY OF CALIFORNIA LOS ANGELES, 595 CHARLES YOUNG DRIVE E, LOS ANGELES, CA 90095, USA

[2]GEOWISSENSCHAFTLICHES ZENTRUM GÖTTINGEN, ABTEILUNG GEOCHEMIE, UNIVERSITÄT GÖTTINGEN, GOLDSCHMIDTSTR. 1, 37077 GÖTTINGEN, GERMANY

[3]INSTITUTE OF ISOTOPE GEOCHEMISTRY AND MINERAL RESOURCES, ETH ZÜRICH, CLAUSIUSSTRASSE 25, 8092 ZÜRICH, SWITZERLAND

[4]DEPARTMENT OF GEOLOGY, UNIVERSITY OF CALIFORNIA DAVIS, ONE SHIELDS AVENUE, DAVIS, CA 95616-8605, USA

[5]DEPARTMENT OF GEOLOGY AND GEOGRAPHY, AUBURN UNIVERSITY, AUBURN, AL 36849, USA

RECEIVED OCTOBER 22, 2009; ACCEPTED MARCH 3, 2010
ADVANCE ACCESS PUBLICATION APRIL 16, 2010

Uranium-series dating of carbonatitic ejecta clasts constrains the crystallization and differentiation timescales of the Laacher See volcano, which erupted 6·3 km^3 of magma (dense rock equivalent) during one of the largest Late Quaternary eruptions in Central Europe. Carbonatites form a distinct population among plutonic ejecta that are present in the middle and late erupted Laacher See tephra. Characteristic trace element patterns of the carbonatites, including negative Eu anomalies, and mantle-like oxygen isotopic compositions preserved in zircon indicate that the Laacher See carbonatites are cogenetic with their phonolite host. Carbonatite U–Th zircon isochron ages range from 32·6 ± 4·1 ka (2σ; MSWD = 1·7; n = 24) to near-eruption age (12·9 ka). Uranium-series carbonatite ages qualitatively agree with alkali feldspar compositions that lack prominent magmatic zonation, but show evidence for perthitic unmixing during subsolidus residence at elevated temperatures (<700°C) in an intrusive carapace surrounding the liquid-dominated interior of the magma system (>720°C). Model differentiation ages and crystallization ages for the carbonatites overlap within a few thousand years as resolved by U–Th dating and indicate rapid crystallization following carbonatite segregation from its parental phonolite. Model differentiation and zircon isochron ages peak at ~17 ka, suggesting a major phase of differentiation of the Laacher See magma system at this time, although the onset of phonolite differentiation dates back to at least ~10–20 kyr prior to eruption. Phenocrysts in the middle and late erupted phonolite magma crystallized shortly before eruption, and the lack of older crystals implies crystal removal through settling or resorption. Crystal ages from both crystal-rich and liquid-dominated parts of a magma system are thus complementary, and reveal different aspects of magma differentiation and residence timescales.

KEY WORDS: *geochronology; Quaternary; carbonatite; uranium series; zircon*

INTRODUCTION

How long is magma stored in subvolcanic reservoirs and how long does it take to evolve to highly differentiated compositions prior to eruption? Answers to these questions are relevant for understanding the pre-eruptive heat and mass transfer that control magmatic diversity and eruptive

*Corresponding author. E-mail: axel@oro.ess.ucla.edu

style, and in developing strategies for magma detection and eruption forecasting. For volcanoes with a history of recurrent eruptions, geophysical sensing can detect the accumulation of magma at depth (Pritchard & Simons, 2002; Wicks *et al.*, 2002), and magma residence times have been estimated from the amount and composition of erupted products assuming that magma input and eruptive output are at steady state (Condomines *et al.*, 1995; Pietruszka & Garcia, 1999). For dormant or monogenetic volcanoes, however, the rates and processes of magma accumulation and storage need to be assessed through petrological and geochronological methods.

The Laacher See eruption 12·9 kyr ago occurred within the East Eifel Volcanic Field (EEVF) and marks a significant geological event during Late Pleistocene times in Central Europe. Different approaches have yielded timescale estimates of several to a few tens of thousand years for the generation and storage of the Laacher See magma prior to eruption. Thermal and fluid dynamical estimates for crystallization and fractionation times within the Laacher See magma chamber are ~3 kyr (Tait *et al.*, 1989), whereas uranium series (U-series) ages for bulk crystal and glass separates range from near-eruption to several tens of thousand years (Bourdon *et al.*, 1994). The generally younger ages obtained for crystals from the phonolites indicate short residence times, whereas some cumulates indicate much longer crystallization timescales (Bourdon *et al.*, 1994). In addition, Bourdon *et al.* (1994) suggested that the Laacher See phonolites evolved from a parental basanite magma via magmatic differentiation over a period of up to 100 kyr. This range of ages reflects in part the duration of processes in different parts of the magma system, but the interpretation of bulk separate crystal ages for phenocryst-poor pumices has been complicated by crystal mixing from the crystal-rich carapace into the liquid-dominated eruptible interior (Bourdon *et al.*, 1994). That this is indeed the case has been demonstrated through crystal-chemical and geochronological analysis of single crystals, which revealed complex crystal populations in the Laacher See phonolite, including crystals dispersed from cooler and more evolved portions of the magma body, solidified precursor intrusions, and wall-rocks (Ginibre *et al.*, 2004; Schmitt, 2006). Guided by these results, we concentrated on single crystal U-series dating combined with whole-rock analysis of plutonic carbonatitic syenite ejecta in the Laacher See pyroclastic deposits to better constrain the timescales and processes of differentiation and crystallization in the Laacher See system. These carbonatitic rocks—the youngest known intrusive carbonatite occurrence worldwide (Woolley & Kjarsgaard, 2008)—are cogenetic with the Laacher See phonolite, highly differentiated, and thus difficult to contaminate. Our results highlight the potential of studying plutonic rocks to elucidate processes of differentiation and duration of pre-eruptive crystallization in youthful volcanic systems (Bacon *et al.*, 2007), and provide evidence for a close genetic link between the Laacher See carbonatites and their evolved phonolite host melt.

EAST EIFEL VOLCANIC FIELD

Late Pleistocene volcanism prior to the Laacher See eruption

Volcanism in the EEVF (Fig. 1) is a part of a series of intra-plate volcanic fields in Central Europe that have been active throughout the Tertiary–Quaternary (Schmincke, 2007, 2008). Tertiary volcanism in the Rhenish Shield and surrounding areas is largely contemporaneous with rifting of the Rhine Graben and broad uplift of pre-Tertiary basement in the Rhenish Shield (Wilson & Downes, 1991; Lustrino & Wilson, 2007). The older Tertiary basaltic lavas are intra-plate alkaline to transitional basalts, such as those of the extensive (600 km^2) 15–16 Ma Vogelsberg shield volcano (Bogaard & Wörner, 2003), in contrast to the younger EEVF highly alkalic and silica-undersaturated magmatism (Mertes & Schmincke, 1983, 1985; Schmincke, 2007).

The EEVF extends over ~400 km^2, and comprises ~100 volcanic centers, dominated by scoria cones and a few maar volcanoes, which mainly erupted silica-undersaturated high-K rocks (Schmincke, 2007, 2008). The three largest volcanic complexes [eruptive volumes of several km^3 dense rock equivalent (DRE)] are the Rieden Complex (leucitites and leucite phonolites), Wehr Volcano (phonolites and trachytes), and Laacher See (compositionally zoned from mafic to evolved phonolite). The oldest Quaternary volcanism in the EEVF (pre-Rieden) occurred at ~600 ka. The Rieden Complex was active between ~450 and 400 ka, and erupted in several phases around a ~2·5 km diameter caldera basin (Bogaard *et al.*, 1989*a*). Volcanism then migrated from west to ESE after a lull in activity between 350 and 215 ka to the Wehr Volcano, about 2 km east of Rieden. The Wehr depression was the source of a ~215 ka silica-saturated trachyte eruption (Hüttenberg tephra), and subsequent minor phonolitic deposits (Glees Tephra) that are dated at ~151 ka (Wörner *et al.*, 1988; Bogaard *et al.*, 1989*b*). Small volumes of phonolitic pumice were also erupted from Dümpelmaar, a small maar-crater that was active around 116 ka (Bogaard *et al.*, 1989*b*). The Dümpelmaar phonolite is compositionally and petrographically very similar to the most recent eruption of the Laacher See. Subsequently, volcanic activity was restricted to a few basanitic to tephritic scoria cones and related lava flows, mostly to the east and south of Wehr, until the eruption of Laacher See.

Laacher See eruption

The Laacher See erupted the most voluminous pyroclastic deposit in the EEVF, representing ~6·3 km^3 (DRE) of

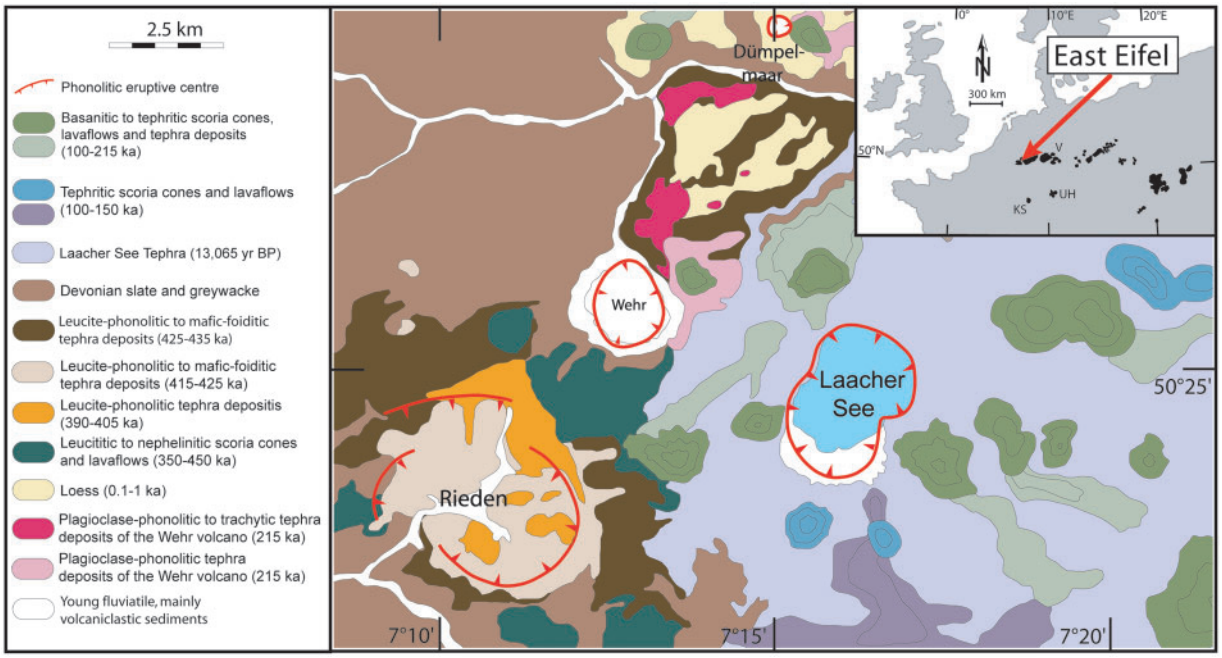

Fig. 1. Geological map of the East Eifel Volcanic Field (EEVF). Inset shows location of the EEVF in the Central European Cenozoic volcanic province. V, Vogelsberg; UH, Urach–Hegau; KS, Kaiserstuhl.

compositionally zoned phonolite (Wörner & Schmincke, 1984*a*, 1984*b*). Near-vent outcrops are a complex succession of phreato-plinian fall and surge deposits, air-fall layers and pyroclastic flows, as well as phreatomagmatic fall, surge and flow deposits towards the end of the eruptive sequence. Distal deposits of the Laacher See eruption formed an ash layer that is widely dispersed in central and eastern Europe (Bogaard & Schmincke, 1984, 1985*a*, *b*; Bogaard *et al.*, 1989*a*, 1989*b*). Because of high sulfur abundances in the Laacher See magma, it affected northern hemisphere climate and human habitats, and is a marker horizon in Greenland ice cores (Schmincke *et al.*, 1999; Riede, 2008). Because of its tephrochronological importance, the chronology of the eruption has been scrutinized extensively and is at present estimated at 12 916 calendar years BP, based on varve and tree ring intercalibrations (Baales *et al.*, 2002). The Laacher See eruption excavated an ~2·5 km diameter crater, now filled by reworked tephra up to a depth of 65 m below the present lake level of Laacher See. Pumice air-fall and ash-flow deposits also temporarily dammed the Rhine River, which eventually catastrophically flooded the Lower Rhine valley (Schmincke *et al.*, 1999; Park & Schmincke, 2009).

Based on characteristic variations in lithology, chemical composition, and eruptive and depositional mechanisms, the Laacher See pyroclastic deposits are subdivided into the Lower (LLST), Middle (MLST) and Upper (ULST-A/B/C) Laacher See tephra units (Bogaard & Schmincke, 1984, 1985). Pumice compositions range from highly evolved, phenocryst-poor (<2% crystals) white phonolite in the LLST deposits to mafic, crystal-rich (up to 55% crystals) gray phonolite in the upper MLST and ULST. The inversion of depositional zonation suggests the existence of a zoned magma body, which was more evolved, crystal-poorer, cooler (~720°C), and more volatile-rich at the top (LLST) than the lower portion of the chamber, which contained more mafic, hotter (at least 840–860°C), less volatile-rich, and more crystalline magma (Wörner & Schmincke, 1984*a*, 1984*b*; Harms & Schmincke, 2000; Berndt *et al.*, 2001; Harms *et al.*, 2004). Volatile-saturation barometry places the top of the magma chamber at ~5–6 km depth, and based on the geometry of the volcanic depression and erupted volumes, the total height of the magma body was ~1–2 km (Wörner & Schmincke, 1984*b*). Lithological variations in the Laacher See deposits also reflect significant changes in eruption mechanisms over the course of the eruption. During the initial Plinian phase, ash and lapilli became dispersed from a ~20 km high eruption column. Conduit-widening (between deposition of the LLST and MLST) led to deposition of pyroclastic flow deposits, and to phreatomagmatic explosions probably triggered by water influx that formed prominent surge deposits in the ULST that are particularly rich in lithic components. Country rocks are sandstones, shales and graywackes of Early Devonian age. The LLST and MLST boundary also marks the appearance of abundant cognate plutonic and cumulate ejecta clasts, which include the relatively rare carbonatitic ejecta studied here.

Laacher See plutonic ejecta

Crystal-rich (<25% glass) cognate cumulate and plutonic rock fragments are found within coarse-grained horizons in the uppermost MLST and ULST deposits. Compositionally, the following groups have been classified (Tait *et al.*, 1989): (1) mafic (clinopyroxene, amphibole, magnetite, apatite); (2) intermediate (plagioclase only, or plagioclase–sanidine-bearing, clinopyroxene, amphibole, magnetite, titanite); (3) syenitic (dominantly sanidine, plagioclase, haüyne).

In addition to these groups of cumulates, rare clasts of intrusive syenite–carbonatite are present in the upper MLST and ULST. Carbonate-bearing syenites in the EEVF have been known since the early 20th century, but the older literature pertaining to the Laacher See 'Gebiet' (= region) deals exclusively with carbonatites from the Rieden Complex (Schuster, 1920; Brauns & Brauns, 1925; Taylor *et al.*, 1967). Laacher See carbonatites *sensu stricto* have only been studied in detail by Liebsch (1996). Compared with the Rieden carbonatites, the Laacher See carbonatites are more evolved and younger (see below). In the following discussion, we refer to the carbonatite nomenclature, petrography, and chemical compositions that were originally presented by Liebsch (1996).

For this study, a representative suite of 11 Laacher See carbonatites (LSC, Fig. 2) was selected, which represent the three major groups that were petrographically classified by Liebsch (1996). Group 1 (calcite-bearing nosean syenites with calcite accumulations; LSC-1) clasts are 129-L and 151-L; Group 2 (syenitic sövites and sövitic syenites; LSC-2) comprises samples 127-L, 222-L, 225-L, 233-L, 337-L, 523-L and 564-L. Clasts 603-L and 604-L belong to Group 3 (calcite-bearing nosean syenites; LSC-3), which differs from Group 1 by the absence of calcite accumulations, and lower overall calcite abundance (<1 vol. %). For comparison, Rieden carbonatite clasts (samples EC-1B, 727-R) were included in this study because they are sufficiently old (as also demonstrated by new U–Pb zircon dates) to have attained U–Th secular equilibrium. Rieden carbonatites thus allow for testing the reliability of *in situ* U–Th zircon geochronology and whole-rock U-series analysis.

ANALYTICAL METHODS

Electron microprobe (EMP)

Major element chemistry for sanidine as well as back-scattered electron (BSE) imaging were performed with a JEOL JXA 8900 RL electron microprobe (EMP) at the Geoscience Center, University of Göttingen. Zonation textures in sanidines were mapped by BSE imaging at a maximum contrast of 0·1 atomic mass units (a.m.u.), and quantified through wavelength-dispersive X-ray spectrometry (WDX) monitoring of 13 elements (Ti, Si, Al, Fe, Ca, Mn, Ba, Mg, Na, K, P, Cl, S). The operating conditions were 15 kV and 15 nA using a 10–20 μm defocused beam. Peak dwell time was 15 s for most elements, except for the low-intensity elements P, Cl, S and Ba, for which the dwell time was increased to 30 s. Backgrounds were measured on both sides of the peaks for 5 s (15 s for P, Cl, S and Ba). Peak overlap of Ti-Kα on Ba-Lα as well as Ba-Lα on Ti-Kα was corrected. Counting statistical errors varied considerably dependent on concentration. For Si the error is <0·6%, for Ba >17%. A second routine program with only eight elements (Si, Al, Fe, Ca, Sr, Na, K, Ba) was applied for standard feldspar analyses at 15 kV acceleration voltage and 20 nA beam current using a 7 μm defocused beam. Peak dwell time was 15 s for high-intensity elements and increased for the low-intensity elements Fe, and Ba plus Sr to 30 and 60 s, respectively. Backgrounds were measured on both sides of the peaks for 5 s (Si, Al, Ca, Na, K), 15 s (Fe), and 30 s (Ba, Sr). Peak overlap of Si-Kα on Sr-Lα was corrected. Relative counting statistical errors range between <0·4% (Si) and >10% (Ba). Alkali loss was checked by varying beam currents and focusing, and found to be insignificant. Standard atomic number, absorption, and fluorescence corrections were applied to all measurements. All analysis spots were documented, and located with respect to growth patterns, by BSE imaging.

Zircon imaging and secondary ion mass spectrometry (SIMS) analysis

Zircon analyses were performed *in situ*, in petrographic thin sections, which has the advantage that the petrographic context of the zircon crystals is preserved. Moreover, sample material for single carbonatite ejecta clasts was frequently limited to centimeter-sized billets, and *in situ* analysis was thus preferable to mineral separation because of potential losses during crushing, sieving, and heavy-liquid separation. Typically three polished petrographic thin sections were prepared for each sample, and zircon was identified and imaged by BSE and cathodoluminescence (CL) methods. Subsequently, zircon-bearing portions were either cored with a 3 mm diameter diamond drill or cut with a diamond saw, and placed on adhesive tape with pre-polished epoxy blocks of standard zircon AS-3 (Paces & Miller, 1993), 91,500 (Wiedenbeck *et al.*, 2004), and Pacoima (Booth *et al.*, 2005). Thin-section pieces and standards were then mounted in a ~2·5 cm diameter epoxy block, ultrasonically cleaned with methanol, and coated with a conductive Au layer of several tens of nanometers thickness.

Secondary ion mass spectrometry (SIMS) analyses of zircon were conducted with three separate analytical set-ups using the UCLA CAMECA ims 1270 to analyze U–Th isotopes (Tables 1 and 2), trace elements [including rare earth elements (REE) and P, Ti, Y, and Hf; Table 2], and oxygen isotopes (Table 3). Analytical procedures

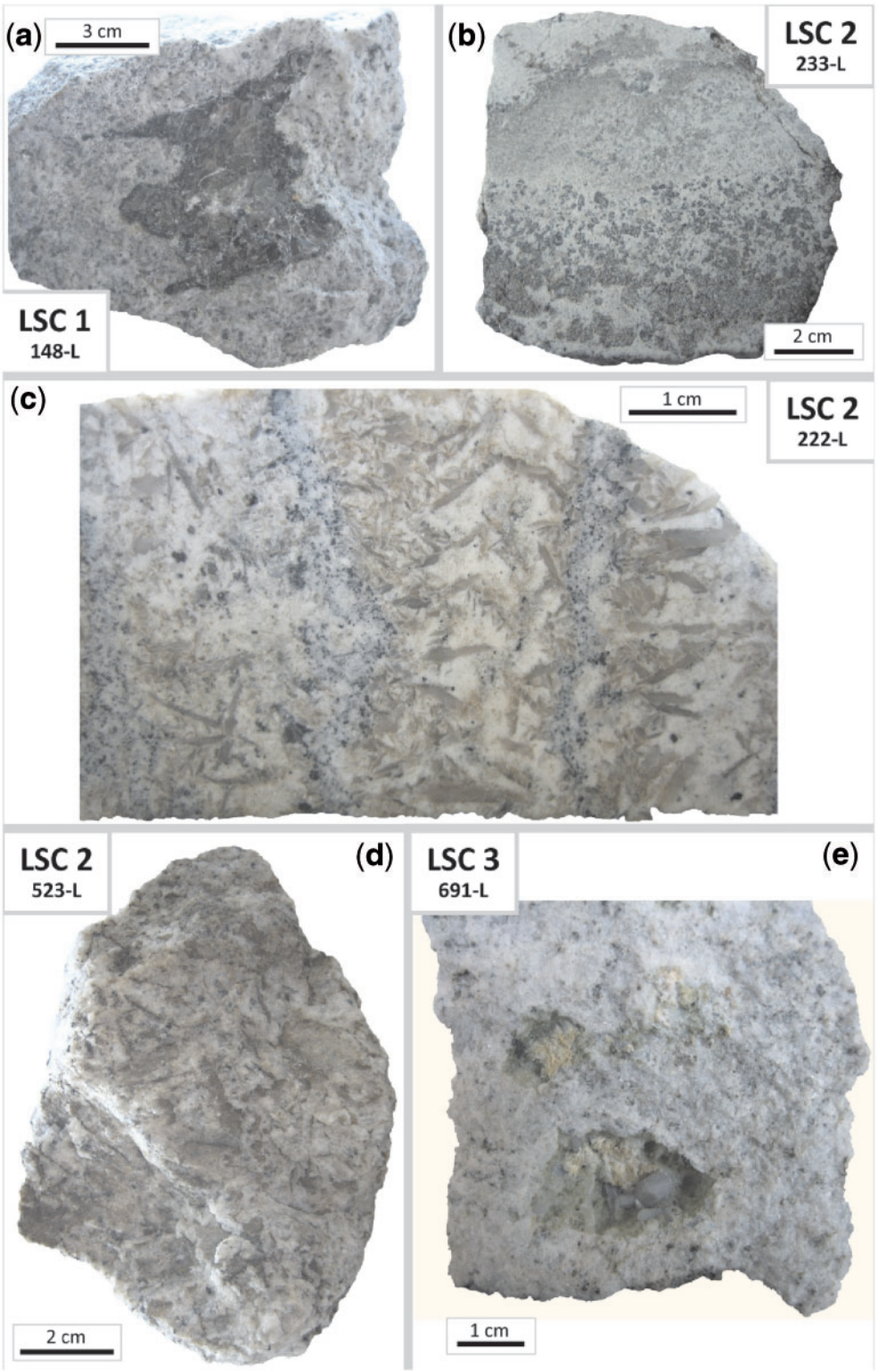

Fig. 2. Carbonatite–syenite xenoliths representative of the various classes present in the Laacher See tephra. (a) 148-L (similar to 129-L): calcite-bearing nosean-syenite with a large (nearly 5 cm), sheared, >99% calcite droplet (sövite) suggesting liquid immiscibility. (b) 233-L: sövite syenite (Group 2) showing magmatic layering with accumulation of coarse nosean and mafic minerals (dark) at the bottom and fine-grained calcite- and sanidine-rich (brown; bright) domains at the top. (c) 222-L: comb-layered sövite syenite (Group 2) consisting of rhythmic layers of bands with mafic minerals (dark), calcite needles and dendrites (brown) alternating with more fine-grained sanidine-rich domains. (d) 523-L: sövitic syenite (Group 2) with elongate calcite (brown). (e) 691-L (similar to 603-L): calcite-bearing nosean-syenite (Group 3) with vugs filled with glass (green), nosean phenocrysts (grey) and calcite needles.

Table 1: SIMS U–Th and trace element analysis of zircon

Sample	Zircon	Spot	(^{238}U)/(^{232}Th)	± (2σ)	(^{230}Th)/(^{232}Th)	± (2σ)	U (ppm)	Th (ppm)	La (ppm)	Ce (ppm)	Pr (ppm)	Nd (ppm)	Sm (ppm)	Eu (ppm)	Gd (ppm)
127-L	5	1	2·91	0·1	1·12	0·18	817	851	0·18	42	0·06	0·64	0·58	0·19	2·9
127-L	5	2	0·312	0·01	0·791	0·066	219	2136	2·7	66	0·26	1·7	1·2	0·47	5·4
127-L	6	1	0·665	0·014	0·829	0·058	855	3904	0·49	561	3·4	36	33	10	125
127-L	6	2	0·707	0·018	0·891	0·066	604	2594	0·2	372	1·6	20	20	6·3	81
127-L	1	1	1·14	0·02	1·04	0·2	143	382	0·16	79	0·33	3·8	4·1	1·3	17
127-L	1	2	1·16	0·06	0·981	0·132	288	752	7	56	0·39	1·6	1	0·38	4·3
127-L	2	1	1·06	0·02	0·912	0·054	1462	4189	0·29	479	2·1	23	24	7·6	91
127-L	2	2	3·72	0·18	1·34	0·24	459	374	0·12	28	0·06	0·4	0·54	0·17	2·2
127-L	3	1	1·34	0·04	0·875	0·228	289	656	4·2	48	0·34	1·5	0·97	0·32	2·3
127-L	3	2	0·985	0·088	0·898	0·114	418	1289	67	211	6·2	18	6·5	1·9	11
127-L	4	1	1·01	0·02	0·888	0·158	201	601	5·9	190	1·6	9·2	6·8	2·1	37
127-L	4	2	1·12	0·04	0·971	0·16	175	476	100	312	21	54	5·6	0·78	6
129-L	Blob	1	15·4	0·6	4·5	1·92	88	17	0·02	27	0·04	0·31	0·17	0·06	0·73
129-L	Fountainpen	1	8·71	0·32	4·05	1·6	48	17	0·02	25	0·04	0·34	0·18	0·1	0·76
129-L	Old School	1	4·25	0·14	1·77	0·12	1243	888	0·27	231	1·3	11	5	1·3	12
129-L	Tank	1	8·83	0·62	3·46	1·4	67	23	0·27	33	0·17	1·3	0·7	0·18	1·4
129-L	Spy	1	3·6	0·26	1·68	0·22	436	368	0·13	31	0·1	0·73	0·6	0·19	2·3
129-L	Mask	1	3·22	0·06	1·56	0·08	2368	2230	9·3	1373	21	147	54	13	88
129-L	Parrot	1	0·704	0·03	0·953	0·052	599	2582	3·4	185	1·7	12	7·9	2·7	25
129-L	Raygun	1	6·68	0·18	2·05	1·44	45	20	0·03	22	0·03	0·28	0·17	0·08	0·59
129-L	Heavyweight	1	4·25	0·08	1·78	0·16	661	472	0·48	192	1·6	14	8·8	2·2	29
129-L	Door	1	1·21	0·02	0·988	0·046	1475	3698	6·4	756	14	89	25	5	39
129-L	Halfmoon	1	1·28	0·08	0·922	0·068	668	1589	0·06	32	0·06	0·37	0·46	0·13	0·97
129-L	Watering Can	1	2·24	0·06	1·19	0·12	1064	1442	0·84	263	2·1	12	3	0·55	3·9
129-L	Watering Can	2	2·97	0·08	1·42	0·12	518	530	0·07	63	0·26	2·6	1·1	0·26	1·9
129-L	Seahorse	1	1·73	0·08	1·15	0·08	803	1409	2·7	247	4·9	28	6·9	1·3	7·2
129-L	Diamond Cut	1	1·06	0·1	0·984	0·096	1018	2916	28	185	3·9	16	7·4	2·1	22
129-L	Torch	1	0·993	0·058	0·955	0·164	570	1741	3·3	111	0·99	6·2	5·1	1·5	16
129-L	1	1	9·12	0·12	2·51	0·74	175	58	0·52	27	0·05	0·43	0·12	0·03	0·83
129-L	2	1	2	0·02	1·31	0·12	461	697	1·4	213	1·1	10	10	4·2	44
129-L	6	1	3·23	0·04	1·64	0·12	707	665	1·1	52	0·31	2·3	1·4	0·32	4·9
129-L	5	1	1·54	0·02	1·18	0·1	360	708	33	272	4·8	28	21	6·7	57
129-L	4	1	0·99	0·034	0·938	0·082	506	1550	0·17	53	0·26	2·5	1·6	0·45	6·3
129-L	3	1	1·03	0·02	0·907	0·076	366	1081	27	588	9·1	66	50	18	141
129-L	7	1	13·7	0·4	4·33	3·98	37	8·2	0·1	87	0·16	1·7	1·5	0·5	4·8
129-L	8	1	3·29	0·18	1·6	0·2	302	278	1·9	98	1·2	10	6·5	1·7	21
151-L	Donut	1	0·51	0·028	0·771	0·072	293	1740	1·5	71	0·65	4·1	2·4	0·55	6·8
151-L	Chimney	1	1·92	0·08	1·03	0·06	1359	2153	0·98	206	2·4	19	13	3·4	42
151-L	Ugly Duckling	1	0·514	0·018	0·802	0·048	452	2664	1·5	141	0·91	7·2	5·5	1·8	19
151-L	Hook	1	0·456	0·096	0·784	0·024	4331	28832	1·3	200	1·4	8·7	4·1	1	15
151-L	Beerbottle	1	1·64	0·1	0·905	0·062	4978	9184	2·2	270	3·7	27	14	3·2	38
151-L	Turtle	1	0·133	0·016	0·801	0·038	366	8338	25	909	24	177	103	27	198
151-L	Pollock	1	7·5	0·22	1·87	0·14	2554	1033	n.a.	n.a.	n.a.	n.a.	n.a.	n.a.	n.a.
151-L	Zippo	1	0·353	0·018	0·769	0·052	272	2336	n.a.	n.a.	n.a.	n.a.	n.a.	n.a.	n.a.
151-L	Zippo	2	0·189	0·006	0·767	0·05	157	2517	n.a.	n.a.	n.a.	n.a.	n.a.	n.a.	n.a.
151-L	Pollock	2	3·79	0·14	1·44	0·28	2291	1833	n.a.	n.a.	n.a.	n.a.	n.a.	n.a.	n.a.
151-L	Pollock	3	2·21	0·2	1·1	0·06	1147	1574	n.a.	n.a.	n.a.	n.a.	n.a.	n.a.	n.a.
151-L	Pollock	4	7·02	0·26	1·82	0·12	1799	777	n.a.	n.a.	n.a.	n.a.	n.a.	n.a.	n.a.
151-L	1	1	0·369	0·004	0·812	0·092	74	612	3·3	69	0·5	2·7	2·3	0·85	7·4
151-L	2	1	1·53	0·04	1	0·1	460	915	0·67	111	0·55	5·3	4·4	1·5	18

(continued)

Table 1: Continued

Sample	Zircon	Spot	(^{238}U)/(^{232}Th)	± (2σ)	(^{230}Th)/(^{232}Th)	± (2σ)	U (ppm)	Th (ppm)	La (ppm)	Ce (ppm)	Pr (ppm)	Nd (ppm)	Sm (ppm)	Eu (ppm)	Gd (ppm)
151-L	3	1	2·82	0·14	1·32	0·1	1593	1713	27	953	16	117	70	19	174
151-L	4	1	0·573	0·006	0·84	0·072	308	1632	0·29	54	0·22	1·7	1·7	0·54	6·9
151-L	5	1	0·89	0·032	0·889	0·114	226	772	0·92	98	0·36	3·1	1·6	0·91	11
222-L	4	1	0·241	0·006	0·771	0·154	370	4659	2184	4823	201	640	185	47	338
222-L	4	2	0·146	0·004	0·749	0·088	528	10994	14	2020	25	185	103	25	251
222-L	1	1	0·768	0·022	0·841	0·102	3399	13427	21	2035	45	345	205	47	465
222-L	1	2	0·853	0·048	0·821	0·08	3452	12284	12	2022	30	226	146	34	354
222-L	5	1	1·01	0·1	0·937	0·15	7059	21255	56	1324	39	222	81	17	134
222-L	6B	1	0·534	0·018	0·848	0·068	7943	45104	132	3501	107	663	278	56	451
222-L	6A	1	1·07	0·08	1·22	0·22	2354	6653	14	1040	17	120	58	12	132
222-L	7	1	0·102	0·004	0·843	0·074	661	19626	44	3604	75	529	237	48	387
225-L	5	1	1·08	0·04	0·997	0·17	1817	5090	52	734	28	142	52	12	111
225-L	5	2	0·304	0·012	0·812	0·084	3566	35549	219	3460	148	734	207	46	291
225-L	7	1	0·908	0·026	0·844	0·152	2357	7881	5·4	814	9·3	79	57	18	167
225-L	7	2	0·604	0·012	0·874	0·14	1731	8700	5·3	1230	14	118	84	25	246
225-L	8	1	0·315	0·006	0·792	0·088	1568	15115	3·5	1386	12	100	80	23	244
225-L	8	2	0·129	0·002	0·823	0·088	682	16024	7·9	1255	11	94	75	22	230
225-L	3	1	0·962	0·028	0·873	0·25	347	1095	2·1	149	0·64	4·5	4·3	1·6	19
225-L	4	1	0·685	0·024	0·83	0·15	279	1238	1·4	152	0·74	6·8	6·4	2·1	24
225-L	1	1	1·17	0·08	0·898	0·144	435	1131	n.a.	n.a.	n.a.	n.a.	n.a.	n.a.	n.a.
225-L	Tin Can	1	1·48	0·08	0·974	0·084	534	1097	n.a.	n.a.	n.a.	n.a.	n.a.	n.a.	n.a.
225-L	Tin Can	2	3·59	0·16	1·31	0·16	1007	852	n.a.	n.a.	n.a.	n.a.	n.a.	n.a.	n.a.
225-L	Tin Can	3	0·366	0·028	0·848	0·088	167	1382	n.a.	n.a.	n.a.	n.a.	n.a.	n.a.	n.a.
225-L	Duck	1	1·04	0·06	1·03	0·12	204	596	n.a.	n.a.	n.a.	n.a.	n.a.	n.a.	n.a.
225-L	Duck	2	0·116	0·004	0·806	0·158	73	1918	n.a.	n.a.	n.a.	n.a.	n.a.	n.a.	n.a.
225-L	Duck	3	3·51	0·44	1·3	0·1	1174	1015	n.a.	n.a.	n.a.	n.a.	n.a.	n.a.	n.a.
233-L	Crowded	1	0·568	0·012	0·782	0·03	3307	17660	17	1133	14	106	81	30	211
233-L	Groupies	1	0·055	0·014	0·75	0·048	136	7502	4·1	452	3·3	25	17	5·7	55
233-L	Middleman	1	1·34	0·1	1·01	0·12	671	1518	6·5	105	2·2	12	4·6	1·1	16
233-L	Thres	1	0·034	0·004	0·781	0·03	229	20453	5	1135	16	120	72	16	152
233-L	Wrench	1	0·081	0·006	0·755	0·036	299	11257	2·9	885	5·9	48	38	13	129
233-L	Teapot	1	0·36	0·012	0·796	0·022	4454	37541	3060	6778	464	1799	534	121	570
233-L	Eagle	1	0·341	0·01	0·777	0·012	5882	52300	80	2199	104	653	287	78	493
233-L	Eagle	3	0·38	0·012	0·793	0·022	3477	27731	202	2019	76	458	210	60	391
233-L	Eagle	4	0·376	0·008	0·797	0·02	4291	34642	80	2199	104	653	287	78	493
233-L	Eagle	2	0·282	0·01	0·768	0·022	13257	142637	307	2556	112	629	268	77	442
233-L	Delta	1	0·113	0·002	0·772	0·084	109	2941	n.a.	n.a.	n.a.	n.a.	n.a.	n.a.	n.a.
233-L	Comb	1	0·074	0·032	0·735	0·118	78	3194	n.a.	n.a.	n.a.	n.a.	n.a.	n.a.	n.a.
233-L	Bowtie	1	0·0198	0·0004	0·758	0·086	116	17876	n.a.	n.a.	n.a.	n.a.	n.a.	n.a.	n.a.
337-L	Footprint	1	1·01	0·06	0·874	0·118	275	826	0·22	96	0·4	2·5	2	0·6	7
337-L	Big M	1	2·06	0·46	1·23	0·28	171	252	1·9	38	0·28	1·1	0·89	0·35	4·1
337-L	Big M	2	1·94	0·56	1·06	0·14	585	914	n.a.	n.a.	n.a.	n.a.	n.a.	n.a.	n.a.
337-L	Big M	3	3·81	0·22	1·46	0·26	749	597	n.a.	n.a.	n.a.	n.a.	n.a.	n.a.	n.a.
337-L	Pentagon	1	1·07	0·06	0·96	0·1	681	1940	7·8	119	1·5	8·3	4·8	1·7	17
337-L	Captains Hat	1	0·16	0·01	0·774	0·126	143	2715	1·9	60	0·31	1·1	0·84	0·36	5·4
337-L	Footprint	2	0·78	0·046	1·02	0·4	37	143	n.a.	n.a.	n.a.	n.a.	n.a.	n.a.	n.a.
337-L	Big M	4	2·29	0·36	1·2	0·2	448	593	n.a.	n.a.	n.a.	n.a.	n.a.	n.a.	n.a.
337-L	3	1	0·42	0·014	0·848	0·064	189	1365	n.a.	n.a.	n.a.	n.a.	n.a.	n.a.	n.a.
523-L	Anteater	1	0·182	0·008	0·753	0·078	45	748	0·4	67	0·3	2·1	2·1	0·64	7·9
523-L	Boss Man	1	0·928	0·016	0·877	0·066	510	1667	0·39	513	2·9	30	29	8·1	98

(continued)

Table 1: Continued

Sample	Zircon	Spot	(^{238}U)/(^{232}Th)	± (2σ)	(^{230}Th)/(^{232}Th)	± (2σ)	U (ppm)	Th (ppm)	La (ppm)	Ce (ppm)	Pr (ppm)	Nd (ppm)	Sm (ppm)	Eu (ppm)	Gd (ppm)
523-L	Lonley Shoe	1	2·47	0·22	1·14	0·18	203	249	85	85	8·2	22	3·4	0·99	7·5
523-L	Boss Man	2	0·59	0·006	0·824	0·022	4918	25274	12	2479	30	219	111	25	241
523-L	Boss Man	3	1·05	0·02	0·878	0·04	2718	7852	1·2	1347	7	65	54	13	177
523-L	Boss Man	4	1·24	0·02	0·887	0·048	2189	5358	0·38	917	4·2	37	34	9·7	123
523-L	Boss Man	5	0·982	0·016	0·893	0·068	983	3039	0·38	514	2·8	29	28	7·5	97
523-L	Lounge Chair	1	6·17	0·24	1·6	0·18	584	287	591	1530	110	262	22	3·4	14
523-L	Lions Roar	1	0·167	0·006	0·816	0·096	26	480	0·39	45	0·21	1·4	1·4	0·49	7·7
523-L	Clinger	1	0·155	0·004	0·708	0·092	22	439	1·1	62	0·36	2·2	1·5	0·54	5·8
523-L	Fishy	1	0·858	0·01	0·899	0·05	2330	8243	1·3	1543	9·2	81	66	17	214
523-L	Horsehead	1	0·422	0·014	0·83	0·024	3232	23237	5·5	1021	14	117	73	18	224
523-L	Lounge Chair	2	9·72	0·28	2·07	0·28	468	146	n.a.	n.a.	n.a.	n.a.	n.a.	n.a.	n.a.
564-L	1	1	2·98	0·43	1·46	0·19	227	231	0·01	6·5	0·01	0·12	0·13	0·04	0·8
564-L	1	2	0·299	0·077	0·854	0·476	11	115	0·02	12	0·02	0·24	0·21	0·09	1·6
564-L	2	1	0·295	0·07	0·787	0·231	13	135	0·01	5·7	0·01	0·09	0·05	0·04	0·57
564-L	2	2	0·213	0·026	0·833	0·073	203	2879	0·04	94	0·17	2·2	4·2	1·1	21
564-L	3	1	0·0836	0·0017	0·861	0·163	3	125	0·14	317	1·4	17	15	3·9	58
564-L	3	2	1·93	0·02	1·02	0·14	1540	2423	0·02	15	0·01	0·17	0·19	0·05	1·1
564-L	4	1	0·011	0·001	0·753	0·066	9	2487	0·03	7·6	0·02	0·05	0·09	0·05	0·77
564-L	4	2	4·44	0·42	1·74	0·5	94	64	0·48	146	0·19	2·4	4·3	1·3	27
564-L	5	2	0·294	0·026	0·795	0·219	38	388	0·18	40	0·1	0·78	1·1	0·32	6·1
603-L	Trapdoor	1	0·064	0·002	0·771	0·132	3·3	157	0·03	12	0·05	0·26	0·49	0·18	3·1
603-L	Warning	1	1·13	0·02	1·01	0·12	115	308	1·8	46	0·3	1·9	1·7	0·61	6·7
603-L	Moonshoe	1	0·481	0·01	0·847	0·152	23	142	4·3	35	0·41	1·7	0·98	0·26	4·3
603-L	Lasergun	1	0·113	0·006	0·687	0·174	10	277	3·5	19	0·38	1·1	0·46	0·12	1·5
603-L	Eagle	1	0·183	0·004	0·618	0·452	1·8	31	n.a.	n.a.	n.a.	n.a.	n.a.	n.a.	n.a.
603-L	Eagle	2	0·0213	0·001	0·763	0·084	2	288	n.a.	n.a.	n.a.	n.a.	n.a.	n.a.	n.a.
603-L	Tetris A	1	1·22	0·06	1·02	0·24	27	67	2·9	95	0·64	4·6	3·3	0·76	10
603-L	Evil Pacman	1	0·423	0·006	0·813	0·066	82	585	0·05	147	0·77	5·9	6·6	2·1	28
603-L	Frankenstein	1	0·071	0·004	0·74	0·092	10	433	n.a.	n.a.	n.a.	n.a.	n.a.	n.a.	n.a.
603-L	Tetris B	1	0·00423	0	0·691	0·022	36	25827	0·55	1198	6·7	42	35	7·4	106
603-L	Evil Pacman	2	0·685	0·014	0·803	0·052	1397	6187	0·26	340	2·4	16	12	3·3	41
604-L	Two-faced	1	0·223	0·008	0·856	0·202	63	859	0·09	606	1·1	7·6	7·2	2·5	30
604-L	Big	1	0·229	0·008	0·846	0·062	305	4041	0·39	2687	6	29	25	7·6	64
604-L	Big	2	0·42	0·016	0·903	0·114	216	1562	0·22	1253	2·8	16	15	4·6	57
604-L	Hangglider	1	0·295	0·016	0·893	0·074	479	4936	0·39	2556	5·1	33	28	8·2	86
604-L	Cupcake	1	0·164	0·006	0·861	0·066	236	4378	n.a.	n.a.	n.a.	n.a.	n.a.	n.a.	n.a.
604-L	Island Chain	1	0·64	0·024	0·905	0·096	1207	5723	2·5	1368	8·7	67	47	10	142
604-L	Rocketship	1	0·408	0·016	0·912	0·112	397	2951	0·3	1415	4·5	16	13	4·1	46
604-L	Blastoff	1	0·077	0·004	0·882	0·09	181	7129	8·8	3781	26	178	105	24	270
604-L	Blastoff	2	0·215	0·008	0·876	0·076	616	8693	n.a.	n.a.	n.a.	n.a.	n.a.	n.a.	n.a.
604-L	Wild One	1	0·415	0·014	0·899	0·102	299	2186	0·29	1745	5	25	20	6·5	74
EC-1B	A	1	7·74	0·17	6·6	1·9	30	12	0·02	2·5	0·01	0·18	0·15	0·09	1
EC-1B	C	1	14·16	0·39	18·9	6·2	13	3	0·05	1·8	0·01	0·14	0·08	0·12	0·82
EC-1B	D	1	1·181	0·025	1·19	0·06	489	1257	0·36	150	2·5	31	30	17	101
EC-1B	E	1	1·93	0·04	1·83	0·09	456	719	0·37	127	2·3	29	30	18	102
EC-1B	K	1	1·67	0·03	1·63	0·07	553	1006	0·49	129	2·7	31	34	19	109

(continued)

Table 1: Continued

Sample	Zircon	Spot	Tb (ppm)	Dy (ppm)	Ho (ppm)	Er (ppm)	Tm (ppm)	Yb (ppm)	Lu (ppm)	Y (ppm)	Ti (ppm)	HfO_2 wt %	P (ppm)	*T* (°C)	Remarks
127-L	5	1	2	38	27	196	64	798	189	936	1·4	0·82	31	589	
127-L	5	2	3·1	47	26	158	48	578	129	874	2	0·77	37	614	
127-L	6	1	52	597	237	1080	249	2324	435	8207	2·7	0·79	60	636	
127-L	6	2	34	408	169	809	193	1828	356	5953	2·1	0·77	50	618	
127-L	1	1	7·3	93	42	214	55	571	120	1435	1·7	1	28	603	
127-L	1	2	2·4	38	22	139	41	485	111	734	2·2	0·95	26	621	
127-L	2	1	38	449	185	872	206	1961	383	6426	2·6	0·67	57	633	
127-L	2	2	1·4	23	15	106	35	449	113	568	1·3	0·82	27	584	
127-L	3	1	2·7	48	30	216	68	790	191	1126	3·9	1·2	61	664	high $^{57}Fe^{+}$
127-L	3	2	7·6	99	49	296	86	981	228	1838	18	1·1	62	804	high $^{57}Fe^{+}$
127-L	4	1	11	139	62	319	80	797	172	2171	4·8	0·82	75	681	
127-L	4	2	1·8	17	6·9	40	11	127	30	238	829	1·1	50	1446	high $^{57}Fe^{+}$
129-L	Blob	1	0·4	5·5	2·6	16	5	55	14	118	3	1	35	644	
129-L	Fountainpen	1	0·28	2·9	1·2	5·8	1·4	15	3·8	58	2·7	0·75	29	636	
129-L	Old School	1	4·1	45	18	87	22	211	46	758	2·9	0·64	37	641	
129-L	Tank	1	0·6	7·6	3·5	19	5·3	61	14	147	1·9	0·88	28	610	
129-L	Spy	1	1·2	18	11	77	28	391	108	447	2·2	0·83	39	621	
129-L	Mask	1	21	178	54	210	43	387	77	2401	3·7	0·6	36	660	
129-L	Parrot	1	9·6	113	51	271	74	830	186	1863	4·9	0·81	47	683	high $^{57}Fe^{+}$
129-L	Raygun	1	0·18	2·6	0·96	5	1·3	14	3·2	47	1·4	0·78	26	589	
129-L	Heavyweight	1	11	135	59	305	78	795	176	2284	4·7	0·8	57	679	
129-L	Door	1	10	95	34	161	40	443	109	1600	2·7	0·65	51	636	
129-L	Halfmoon	1	0·46	6·6	3·5	21	6·4	82	23	147	3	0·83	47	644	
129-L	Watering Can	1	0·91	7·8	2·2	9·5	2·3	27	6·6	123	14	0·64	48	778	
129-L	Watering Can	2	0·52	4·5	1·7	8·7	2·3	27	7·8	94	8·6	0·88	47	732	
129-L	Seahorse	1	1·6	13	3·7	16	4·1	44	12	197	2·1	0·8	42	618	
129-L	Diamond Cut	1	8·6	119	56	319	90	970	216	2112	4·2	0·78	63	670	high $^{57}Fe^{+}$
129-L	Torch	1	6·4	78	35	180	49	510	111	1227	6·3	0·78	47	704	
129-L	1	1	0·13	3	1	4·6	1·3	13	3·5	45	1·5	0·69	9·7	594	
129-L	2	1	17	219	96	491	125	1212	272	3398	4·1	0·75	30	668	
129-L	6	1	1·9	24	11	60	16	167	40	5576	5·2	0·8	8·8	688	
129-L	5	1	18	205	81	376	100	981	206	427	4·6	0·74	36	678	
129-L	4	1	2·4	26	10	56	15	150	36	2781	5	0·81	16	685	
129-L	3	1	44	477	178	773	177	1672	306	460	5·8	0·62	45	697	
129-L	7	1	1·9	20	9·3	44	12	103	25	386	3·3	0·73	6·9	651	
129-L	8	1	7·6	88	39	216	61	643	156	1564	3·1	0·74	20	646	
151-L	Donut	1	2·3	27	11	55	14	153	33	414	1·7	1·1	58	603	
151-L	Chimney	1	16	177	70	340	89	884	180	2756	2·6	0·71	62	633	
151-L	Ugly Duckling	1	7·3	93	39	198	53	565	121	1416	2·7	0·78	58	636	
151-L	Hook	1	7·4	110	51	274	74	761	142	2571	2·1	0·78	53	618	
151-L	Beerbottle	1	14	185	89	537	163	1871	401	4216	6·4	0·65	93	705	
151-L	Turtle	1	55	481	144	529	109	914	145	5715	42	1·6	71	901	high $^{57}Fe^{+}$
151-L	Pollock	1	n.a.	n.a.	n.a.	n.a.	n.a.	n.a.	n.a.	n.a.	n.a.	n.a.	n.a.	n.a.	
151-L	Zippo	1	n.a.	n.a.	n.a.	n.a.	n.a.	n.a.	n.a.	n.a.	n.a.	n.a.	n.a.	n.a.	
151-L	Zippo	2	n.a.	n.a.	n.a.	n.a.	n.a.	n.a.	n.a.	n.a.	n.a.	n.a.	n.a.	n.a.	
151-L	Pollock	2	n.a.	n.a.	n.a.	n.a.	n.a.	n.a.	n.a.	n.a.	n.a.	n.a.	n.a.	n.a.	
151-L	Pollock	3	n.a.	n.a.	n.a.	n.a.	n.a.	n.a.	n.a.	n.a.	n.a.	n.a.	n.a.	n.a.	
151-L	Pollock	4	n.a.	n.a.	n.a.	n.a.	n.a.	n.a.	n.a.	n.a.	n.a.	n.a.	n.a.	n.a.	
151-L	1	1	3	38	16	81	22	217	53	593	2·6	1	5·5	633	
151-L	2	1	7·2	91	40	208	53	516	119	1518	7·3	0·59	13	717	

(continued)

Table 1: Continued

Sample	Zircon	Spot	Tb (ppm)	Dy (ppm)	Ho (ppm)	Er (ppm)	Tm (ppm)	Yb (ppm)	Lu (ppm)	Y (ppm)	Ti (ppm)	HfO_2 wt %	P (ppm)	*T* (°C)	Remarks
151-L	3	1	55	597	220	996	244	2341	420	8258	2·9	0·62	44	641	
151-L	4	1	3·2	46	24	148	44	474	120	886	7	0·56	16	713	
151-L	5	1	5·7	91	53	330	95	940	213	2128	2·6	1	12	633	
222-L	4	1	96	879	274	1081	244	2388	408	11476	11	1·3	230	755	high $^{57}Fe^{+}$
222-L	4	2	82	786	268	1128	262	2451	471	12105	19	1·3	107	810	
222-L	1	1	152	1518	528	2231	505	4715	849	17257	9·4	0·61	159	740	
222-L	1	2	126	1260	440	1884	432	4136	762	15410	5·3	0·66	149	689	high $^{57}Fe^{+}$
222-L	5	1	42	422	158	724	173	1636	305	6428	21	0·88	113	821	high $^{57}Fe^{+}$
222-L	6B	1	130	1125	338	1294	276	2448	436	13089	22	1	114	826	
222-L	6A	1	43	421	146	615	138	1252	242	5675	28	0·99	71	853	
222-L	7	1	109	884	253	948	200	1751	329	11028	6·1	1·4	99	701	
222-L	Dodo	1	33	353	132	563	125	1092	202	5147	5·5	1·1	60	693	
225-L	5	1	33	335	128	588	141	1349	268	4506	42	1	89	901	high $^{57}Fe^{+}$
225-L	5	2	86	804	260	1056	225	1957	356	9167	36	1	83	882	high $^{57}Fe^{+}$
225-L	7	1	61	667	257	1183	286	2720	530	9202	10	1	112	746	high $^{57}Fe^{+}$
225-L	7	2	88	936	348	1532	350	3171	599	12138	5·9	1	97	698	
225-L	8	1	91	952	339	1432	325	2988	545	12041	5·1	0·84	75	686	
225-L	8	2	88	932	333	1404	319	2897	527	11544	4·6	1·1	74	678	
225-L	3	1	9·3	130	66	383	109	1239	259	2207	2·3	0·68	82	624	
225-L	4	1	11	136	62	332	87	918	194	2143	2·9	0·87	50	641	
225-L	1	1	n.a.	n.a.	n.a.	n.a.	n.a.	n.a.	n.a.	n.a.	n.a.	n.a.	n.a.	n.a.	
225-L	Tin Can	1	n.a.	n.a.	n.a.	n.a.	n.a.	n.a.	n.a.	n.a.	n.a.	n.a.	n.a.	n.a.	
225-L	Tin Can	2	n.a.	n.a.	n.a.	n.a.	n.a.	n.a.	n.a.	n.a.	n.a.	n.a.	n.a.	n.a.	
225-L	Tin Can	3	n.a.	n.a.	n.a.	n.a.	n.a.	n.a.	n.a.	n.a.	n.a.	n.a.	n.a.	n.a.	
225-L	Duck	1	n.a.	n.a.	n.a.	n.a.	n.a.	n.a.	n.a.	n.a.	n.a.	n.a.	n.a.	n.a.	
225-L	Duck	2	n.a.	n.a.	n.a.	n.a.	n.a.	n.a.	n.a.	n.a.	n.a.	n.a.	n.a.	n.a.	
225-L	Duck	3	n.a.	n.a.	n.a.	n.a.	n.a.	n.a.	n.a.	n.a.	n.a.	n.a.	n.a.	n.a.	
233-L	Crowded	1	78	837	313	1362	313	2961	537	10218	20	1	62	815	
233-L	Groupies	1	22	248	102	470	112	1034	207	3489	5·5	1·1	22	693	
233-L	Middleman	1	6·8	105	60	370	107	1109	259	2044	11	0·88	39	755	
233-L	Thres	1	48	434	137	538	123	1166	214	5485	5	0·9	24	685	
233-L	Wrench	1	55	639	261	1217	290	2624	520	8658	4·7	1·3	65	679	
233-L	Teapot	1	172	1452	421	1573	326	2847	485	13729	549	0·84	182	1342	high $^{57}Fe^{+}$
233-L	Eagle	1	154	1445	474	1894	414	3638	650	14892	7101	0·88	148	2308	high $^{57}Fe^{+}$
233-L	Eagle	3	126	1240	425	1785	399	3622	655	13645	29	0·99	114	857	high $^{57}Fe^{+}$
233-L	Eagle	4	154	1445	474	1894	414	3638	650	14014	166	0·97	188	1102	high $^{57}Fe^{+}$
233-L	Eagle	2	141	1332	439	1760	384	3457	603	14317	39	0·85	130	892	high $^{57}Fe^{+}$
233-L	Delta	1	n.a.	n.a.	n.a.	n.a.	n.a.	n.a.	n.a.	n.a.	n.a.	n.a.	n.a.	n.a.	
233-L	Comb	1	n.a.	n.a.	n.a.	n.a.	n.a.	n.a.	n.a.	n.a.	n.a.	n.a.	n.a.	n.a.	
233-L	Bowtie	1	n.a.	n.a.	n.a.	n.a.	n.a.	n.a.	n.a.	n.a.	n.a.	n.a.	n.a.	n.a.	
337-L	Footprint	1	2·8	35	16	79	21	206	44	586	1·7	1·3	11	603	
337-L	Big M	1	2·1	32	19	128	39	493	126	655	7·6	0·9	11	721	
337-L	Big M	2	n.a.	n.a.	n.a.	n.a.	n.a.	n.a.	n.a.	n.a.	n.a.	n.a.	n.a.	n.a.	
337-L	Big M	3	n.a.	n.a.	n.a.	n.a.	n.a.	n.a.	n.a.	n.a.	n.a.	n.a.	n.a.	n.a.	
337-L	Pentagon	1	6·7	78	34	173	44	439	95	1185	8·9	0·69	9·2	735	
337-L	Captains Hat	1	3·4	65	37	228	64	668	146	1433	3·1	1·7	11	646	
337-L	Footprint	2	n.a.	n.a.	n.a.	n.a.	n.a.	n.a.	n.a.	n.a.	n.a.	n.a.	n.a.	n.a.	
337-L	Big M	4	n.a.	n.a.	n.a.	n.a.	n.a.	n.a.	n.a.	n.a.	n.a.	n.a.	n.a.	n.a.	
337-L	3	1	n.a.	n.a.	n.a.	n.a.	n.a.	n.a.	n.a.	n.a.	n.a.	n.a.	n.a.	n.a.	
523-L	Anteater	1	3·6	51	24	135	38	407	92	783	1·9	1·4	7·7	610	
523-L	Boss Man	1	39	434	161	707	165	1498	295	5862	1·9	0·88	34	610	

(continued)

Table 1: Continued

Sample	Zircon	Spot	Tb (ppm)	Dy (ppm)	Ho (ppm)	Er (ppm)	Tm (ppm)	Yb (ppm)	Lu (ppm)	Y (ppm)	Ti (ppm)	HfO_2 wt %	P (ppm)	*T* (°C)	Remarks
523-L	Lonley Shoe	1	3·3	54	28	165	45	476	109	1016	2·2	0·92	17	621	high $^{57}Fe^{+}$
523-L	Boss Man	2	83	821	289	1208	266	2326	450	9737	11	0·62	41	755	
523-L	Boss Man	3	70	751	283	1227	285	2540	505	10212	2·6	0·73	52	633	
523-L	Boss Man	4	50	570	222	978	232	2120	426	8012	2·6	0·8	41	633	
523-L	Boss Man	5	39	425	161	717	162	1509	298	5826	1·8	0·87	32	607	
523-L	Lounge Chair	1	5·8	44	19	127	41	476	118	695	7096	0·8	15	2308	high $^{57}Fe^{+}$
523-L	Lions Roar	1	3·9	54	24	123	33	340	73	920	1·5	1·5	14	594	
523-L	Clinger	1	2·6	32	15	75	20	213	48	501	2·3	1·6	6·1	624	
523-L	Fishy	1	83	923	351	1557	359	3229	647	12013	3·6	0·67	63	658	
523-L	Horsehead	1	79	855	332	1497	353	3149	628	11904	7·3	0·59	80	717	
523-L	Lounge Chair	2	n.a.	n.a.	n.a.	n.a.	n.a.	n.a.	n.a.	n.a.	n.a.	n.a.	n.a.	n.a.	
564-L	1	1	0·48	7·2	4·1	27	9·3	110	29	149	1·6	1·8	9·6	598	
564-L	1	2	0·89	13	7·3	46	15	164	42	261	1·1	1·3	7·9	573	
564-L	2	1	0·41	6·2	3·5	21	7·1	81	21	127	1	1·8	7·6	567	
564-L	2	2	9·8	143	70	392	111	1141	253	2606	1·3	1·4	17	584	
564-L	3	1	23	267	110	534	134	1298	279	4063	1·5	0·66	21	594	
564-L	3	2	0·54	8·7	4·4	27	8·1	91	22	178	1·4	0·75	9·6	589	
564-L	4	1	0·39	6·6	3·7	24	7·5	89	23	3887	1·5	1·5	28	594	
564-L	4	2	13	192	99	581	168	1785	399	129	1·2	1·1	9·9	579	
564-L	5	2	2·7	40	20	119	33	356	82	783	2·4	0·77	9·8	627	
603-L	Trapdoor	1	1·9	29	17	114	36	451	109	552	2·1	1·3	12	618	
603-L	Warning	1	3·5	44	20	107	29	315	69	663	1·5	1·5	7·4	594	
603-L	Moonshoe	1	1·7	26	11	64	19	196	45	401	1·8	1·5	7·6	607	
603-L	Lasergun	1	1·1	18	9·1	58	17	190	43	319	8·5	1·5	8·6	731	high $^{57}Fe^{+}$
603-L	Eagle	1	n.a.	n.a.	n.a.	n.a.	n.a.	n.a.	n.a.	n.a.	n.a.	n.a.	n.a.	n.a.	
603-L	Eagle	2	n.a.	n.a.	n.a.	n.a.	n.a.	n.a.	n.a.	n.a.	n.a.	n.a.	n.a.	n.a.	
603-L	Tetris A	1	4·2	48	19	91	23	227	48	684	3·3	0·84	6·8	651	
603-L	Evil Pacman	1	13	174	81	427	116	1194	258	2685	1·4	1·1	15	589	
603-L	Frankenstein	1	n.a.	n.a.	n.a.	n.a.	n.a.	n.a.	n.a.	n.a.	n.a.	n.a.	n.a.	n.a.	
603-L	Tetris B	1	49	567	218	972	225	2072	383	7495	5·2	1·6	58	688	
603-L	Evil Pacman	2	17	207	86	414	102	958	205	2858	5·2	0·87	13	688	
604-L	Two-faced	1	14	171	73	354	90	901	184	2774	1·7	0·99	16	603	
604-L	Big	1	35	391	152	682	160	1500	292	5547	4·8	0·71	41	681	
604-L	Big	2	25	284	114	509	121	1118	221	4267	4·1	0·76	29	668	
604-L	Hangglider	1	40	434	170	758	175	1636	316	6077	4·8	0·75	30	681	
604-L	Cupcake	1	n.a.	n.a.	n.a.	n.a.	n.a.	n.a.	n.a.	n.a.	n.a.	n.a.	n.a.	n.a.	
604-L	Island Chain	1	49	525	200	877	202	1822	359	7146	12	0·62	48	763	
604-L	Rocketship	1	21	246	98	449	106	1008	197	3765	4	0·8	25	666	
604-L	Blastoff	1	90	912	330	1428	325	2896	563	11707	8·2	0·59	74	727	
604-L	Blastoff	2	n.a.	n.a.	n.a.	n.a.	n.a.	n.a.	n.a.	n.a.	n.a.	n.a.	n.a.	n.a.	
604-L	Wild One	1	32	376	150	685	165	1603	310	5666	2·8	0·68	30	639	
EC-1B	A	1	0·47	5·4	2·6	12	3·4	35	8·2	76	1·5	0·67	4·2	594	
EC-1B	C	1	0·4	5·7	2·4	12	2·9	27	6·5	71	2·2	0·76	3·2	621	
EC-1B	D	1	31	298	102	386	75	577	110	2774	8·1	0·71	18	726	
EC-1B	E	1	36	374	130	518	106	845	158	3533	4·6	0·72	48	678	
EC-1B	K	1	39	393	136	542	110	901	164	3603	5·3	0·74	55	689	

Activities calculated using the Cheng *et al.* (2000) decay constant of $\lambda(^{230}Th) = 9{\cdot}15771 \times 10^{-6}$. Other decay constants from Jaffey *et al.* (1971) Ti-in-zircon temperatures for $a(TiO_2) = a(SiO_2)$ using the calibration of Ferry & Watson (2007). n.a., not analyzed.

Table 2: Summary of SIMS U–Th zircon isochron ages

Sample	Type	m	± (2σ)	$(^{230}Th)/(^{232}Th)_0$	± (2σ)	Age	+ (2σ)	− (2σ)	MSWD	n
127-L	LSC 2	0·149	0·025	0·887	0·015	17·6	3·3	−3·2	0·52	12
129-L	LSC 1	0·259	0·028	0·941	0·045	32·7	4·2	−4·1	1·7	24
151-L	LSC 1	0·157	0·017	0·868	0·025	18·6	2·2	−2·2	1·8	17
222-L	LSC 2	0·114	0·170	0·881	0·160	13·2	23	−19	2·0	9
225-L	LSC 2	0·147	0·030	0·911	0·034	17·4	3·9	−3·8	0·5	15
233-L	LSC 2	0·091	0·052	0·828	0·030	10·4	6·4	−6·1	1·3	13
337-L	LSC 2	0·180	0·056	0·924	0·050	21·7	7·7	−7·2	0·91	9
523-L	LSC 2	0·132	0·020	0·870	0·015	15·5	2·5	−2·5	0·45	13
564-L	LSC 2	0·192	0·049	0·949	0·059	23·3	6·8	−6·4	0·52	9
603-L	LSC 3	0·217	0·061	0·889	0·061	26·7	8·9	−8·2	1·03	11
604-L	LSC 3	0·099	0·180	0·943	0·135	11·4	24	−20	0·19	10
EC-1B	Rieden	0·893	0·240	1·243	1·222	244	∞	−82	1·5	5

LSC, Laacher See carbonatite group. Activities calculated using the Cheng *et al.* (2000) decay constant of $\lambda(^{230}Th) = 9{\cdot}15771 \times 10^{-6}$. $m = (^{230}Th)/(^{232}Th)$ vs $(^{238}U)/(^{232}Th)$ isochron slope. $(^{230}Th)/(^{232}Th)_0$ = initial ratio. MSWD, mean square of weighted deviates; n, number of zircon spot analyses in regression; ∞, secular equilibrium.

Table 3: Summary of SIMS oxygen isotope analysis of zircon

Sample	Type	$\delta^{18}O$ (‰)	± (1 SD)	n
129-L	LSC 1	5·94	0·39	8
151-L	LSC 1	5·74	0·37	5
225-L	LSC 2	4·73	0·41	29
337-L	LSC 2	5·77	0·36	6
564-L	LSC 2	5·05	0·36	15
603-L	LSC 3	5·17	0·25	5
604-L	LSC 3	5·02	0·14	10
EC-1B	Rieden	4·90	0·29	15

SD, standard deviation of multiple spot analyses; n, number of spot analyses. All values relative to SMOW ($^{18}O/^{16}O = 2{\cdot}00520 \times 10^{-3}$; Baertschi, 1976).

followed those published by Schmitt (2006) for U–Th, Monteleone *et al.* (2007) for trace elements, and Trail *et al.* (2007) for oxygen isotopes. During trace element analysis, additional isotopes (^{26}Mg, ^{55}Mn, ^{57}Fe) were also monitored to detect beam overlap onto other crystals, but not quantified because of lack of suitable zircon standards. Trace element relative sensitivity factors were determined by normalization to $^{30}Si^+$ using NIST SRM 610 glass as a standard (Pearce *et al.*, 1995), except for Ti, which was calibrated on SL-13 zircon with a Ti abundance of 6·32 ppm (Harrison *et al.*, 2007). Accuracy was confirmed by replicate analysis of 91500 zircon (Wiedenbeck *et al.*, 2004) for which abundances were within ±6% of the published average values for heavy REE (HREE) and Ce, and between ±10–20% for other light REE (LREE). La abundances in 91500 zircon scatter by ~65%, but the average value is well within the range of published laser ablation inductively coupled plasma mass spectrometry (LA-ICPMS) and SIMS data. We also report HfO_2 for 91500 (average 0·71 ±0·01 wt %) in agreement with published working values, and average Ti abundances of 4·7 ± 0·4 ppm (minimum 4·1 ppm, maximum 5·9 ppm) and P abundance of 38 ± 8 ppm (minimum 27 ppm, maximum 58 ppm) for 91500 zircon (see Supplementary Data, available for downloading at http://www.petrology.oxfordjournals.org/).

Inclusion-free areas were targeted using reflected light microscopic and SEM imagery. In some instances, U–Th analyses were affected by accidental sputtering of calcite inclusions, which were invisible at the surface in the reflected light microscopic image used to target the ion beam during SIMS analysis, but which were encountered during excavation of the sputter crater (typically ~2–5 μm deep). In these cases, a cluster ion of $^{232}Th_2CO^{2+}$ at mass/charge = 246 a.m.u. interfered with $^{230}Th^+O$, which would require a mass resolution of $m/\Delta m = 30{,}000$ to resolve it from $^{230}Th^+O$. Because this is beyond the practical range of the ims 1270, we instead monitored beam overlap onto calcite by analyzing mass/charge = 244 a.m.u. ($^{232}ThC^+$). Runs that showed elevated

244 intensities were discarded. Trace element analysis spots in subsequent analysis sessions were superimposed onto the U–Th spots (Table 1). For oxygen isotopic analysis, spots were placed adjacent to U–Th and trace element spots to avoid contamination from ^{16}O implanted by the primary ion beam used for U–Th and trace element analysis.

Whole-rock analysis

Whole-rock and glass powders were dissolved at either UCLA or UC Davis using a mixture of concentrated HF and HNO_3 on a hotplate in Savillex beakers, followed by evaporation and treatment with 6N HCl and final dissolution in HNO_3 for column chemistry. Column chemistry and mass spectrometry for analysis of U and Th isotopic composition and concentration were performed at UC Davis following procedures detailed by Cooper & Donnelly (2008). In brief, after dissolution samples were split into two aliquots. One aliquot was spiked with ^{229}Th and ^{233}U for isotope dilution analysis, the second aliquot was unspiked and used for measurement of the U and Th isotopic composition. After sample–spike equilibration, both aliquots were dried and redissolved in 7N HNO_3 for column chemistry. The chemical separation procedure was the same for both isotope dilution and isotopic composition aliquots: U and Th were separated from the rock matrix by ion-exchange chromatrography using Eichrom TRU resin. After loading the samples on the column, major and other trace elements were washed from the column using 7M HNO_3, 1·5M HNO_3, and 3M HCl. U was eluted from the column in 0·1M HCl + trace HF, and Th was eluted from the column in 0·2M HCl.

Following purification of U and Th, samples were analyzed using a Nu Plasma multicollector (MC)-ICPMS system housed in the UC Davis Interdisciplinary Center for Plasma Mass Spectrometry, following procedures detailed by Cooper & Donnelly (2008). Mass bias and relative Faraday-ion counter gain were calibrated using NIST CRM 112A for both Th and U analyses; although Th and U are known to have slightly different mass bias during MC-ICPMS analyses (Sims *et al.*, 2008), this effect differs from instrument to instrument and our ability to reproduce the Th isotopic compositions of rock and solution standards (see below) indicates that any differential mass bias between U and Th was a minor contributor to overall uncertainty of the measurements. Data accuracy and reproducibility were assessed by running solution and rock standards as unknowns during the same analysis sessions, and by replicating several samples. Measured $^{230}Th/^{232}Th$ ratios for solution standards (OU Th and WUN Th standards) were within 0·5% of their accepted values (Sims *et al.*, 2008). Rock standard TML was processed through chemical separation in parallel with the samples, and the $(^{230}Th)/(^{238}U)$ values of two separate aliquots of TML were within 0·4% and 1·7%, respectively, of secular equilibrium (Table 4), indicating that the combined error on measurements of Th and U concentrations and Th isotopic composition, including all errors in spike calibration, weighing error, and analytical uncertainties, was less than 1·7%. Replicate analyses of three samples (225-La, 225-Lb, and 1034M) were included in the analyses. Separate aliquots of the sample powders were dissolved, processed through the chemical separations, and analyzed; replicates are labeled with the suffix 'R' in Table 4. Replicate analyses of U and Th concentrations and U and Th isotopic compositions for the glass sample 1034M were within 0·5% of each other. Larger differences between replicates of 225-L can be attributed to the presence of accessory phases in the powders and 'nugget effects' on dissolution (see discussion in Results below). Samples 1002M and 1034M are phonolitic glasses previously analyzed for U-series disequilibria (Bourdon *et al.*, 1994). Our new analyses compare favorably with the previous analyses; although there are some differences in Th and U concentrations (up to 2·8% difference), which could be attributed to heterogeneity within the sample powders, whereas our measurements of Th isotopic compositions and $(^{230}Th)/(^{238}U)$ are in excellent agreement (within ~1%) with the previous measurements.

RESULTS

Petrography and compositions

Nomenclature

Carbonatites are magmatic rocks with >50% calcite (Streckeisen, 1979); use of the terminology 'carbonatitic' or 'calcite-bearing' implies lower calcite contents. For simplicity, we use the term carbonatite here independent of calcite abundance. The Laacher See carbonatites and carbonatitic rocks (LSC) are coarse-grained calcite-carbonatite sövites. We texturally and compositionally distinguish three types of LSC rocks: calcite-bearing nosean-syenites with rounded nearly 100% sövite domains up to 5 cm in diameter (group LSC-1), sövite-syenites (group LSC-2), and calcite-bearing nosean-syenites (group LSC-3). All three groups largely consist of varying proportions of calcite (<1–76 vol. %), sanidine (8–89 vol. %), and nosean (3–50 vol. %). Further constituents such as clinopyroxene, biotite, albite and garnet occur sporadically. The heavy mineral assemblage is dominated by magnetite, zircon, and apatite, plus rare cpyrochlore and titanite. Trace amounts of rhodochrosite, cancrinite, allanite, and baddeleyite are occasionally present. Vesicular interstitial glass occurs in nearly every rock but does not usually exceed 2 vol. %. Vugs are prevalent and can contain glass and euhedral minerals (especially sanidine, nosean, biotite; Fig. 2, 691-L). Cumulate textures and modal layering are common (Fig. 2).

Table 4: Summary of U-series analysis of whole-rocks

Sample no.	Unit	U (ppm)	Th (ppm)	Th/U	$(^{230}Th)/(^{232}Th)$	$(^{238}U)/(^{232}Th)$	$(^{230}Th)/(^{238}U)$	$(^{234}U)/(^{238}U)$	Model age (ka)	± (2σ)
151-La	LSC 1	5·47	9·47	1·73	1·010	1·758	0·575	1·006	19·4	5·2
151-Lb	LSC 1	2·36	7·72	3·28	0·869	0·929	0·936	1·041	13·7	24·8
225-La	LSC 2	10·1	7·81	0·773	1·284	3·937	0·326	1·002	16·1	3·2
225-Lb	LSC 2	40·4	31·2	0·774	1·271	3·932	0·323	1·001	15·6	3·2
225-La R	LSC 2	13·4	9·01	0·671	1·383	4·533	0·305	1·001	16·7	3·1
225-Lb R	LSC 2	41·8	32·7	0·782	1·283	3·891	0·330	1·002	16·3	3·2
337-La	LSC 2	7·88	17·7	2·24	0·943	1·358	0·694	1·008	19·0	7·2
337-Lab	LSC 2	13·4	35·9	2·67	0·903	1·139	0·793	1·004	17·2	10·4
603-L	LSC 3	13·1	19·4	1·48	1·060	2·054	0·516	0·999	19·7	4·5
604-L	LSC 3	10·4	18·3	1·76	0·973	1·728	0·563	1·000	15·0	5·1
1002	Lower Laacher See Tephra, glass	26·3	94·8	3·60	0·863	0·844	1·022	1·017	–	–
1034-M	Middle Laacher See Tephra, glass	8·31	31·4	3·78	0·869	0·805	1·079	0·999	–	–
1034-M R	Middle Laacher See Tephra, glass	8·30	31·4	3·78	0·866	0·805	1·075	1·002	–	–
712-R	Rieden	6·29	17·2	2·73	1·125	1·115	1·009	1·003	–	–
727-R	Rieden	4·07	11·5	2·82	1·112	1·080	1·030	1·030	–	–
TML-LS1	Table Mountain Latite	11·0	31·0	2·81	1·077	1·084	0·993	1·003	–	–
TML-LS2	Table Mountain Latite	11·1	31·7	2·86	1·082	1·064	1·017	1·002	–	–

R, replicate. LSC, Laacher See carbonatite group. Based on analysis of rock and solution standards, 2σ measurement uncertainties for Th and U concentrations are ~1%, Th isotopic ratios are better than 1%, and U isotopic ratios are ~0·6%. Model ages are calculated with 1034 glass composition $(^{230}Th)/(^{232}Th) = 0{\cdot}855 \pm 0{\cdot}008$ and $(^{238}U)/(^{232}Th) = 0{\cdot}812 \pm 0{\cdot}006$ as parent from Bourdon *et al.* (1994) recalculated using the Cheng *et al.* (2000) decay constant $\lambda(^{230}Th) = 9{\cdot}15771 \times 10^{-6}$. Other decay constants from Jaffey *et al.* (1971).

Group 1 clasts are characterized by the presence of nearly 100% pure round calcite domains up to 10 cm in diameter (Fig. 2a, 148-L, which is equivalent to 129-L and 151-L). These are surrounded by a margin rich in clinopyroxene, sanidine, biotite, magnetite, and apatite. These nearly pure calcite domains resemble droplets and suggest that two chemically different melts coexisted (Fig. 2a). In contrast, Groups 2 and 3 show textural evidence for a co-precipitation of silicates and calcite (Fig. 2 b–e, 222-L, 222-L, 523-L; 691-L). Sanidine sheaves and comb-layering indicate relatively fast cooling rates and/or supersaturation of sanidine components in the melt. Sinuous grain boundaries, a textural feature of near-eutectic growth, are common in these samples (Fig. 3). Group 3 carbonatites have the lowest modal abundances of calcite (<5 vol. %, Fig. 2e, 691-L, equivalent to 603-L and 604-L). Along with calcite, sanidine and nosean, albite occurs in significant abundance (up to 31 vol. %).

Silicate–calcite textural relations are complex, as illustrated by selected BSE images for different types of carbonate–silicate intergrowths in Group 1–3 carbonatites (Fig. 3). Calcite and silicate minerals are always closely intergrown, sometimes indicating eutectic growth relations. Sample 337-L is different from most of the other samples. Accessory apatite, pyrochlore and zircon are unusually enriched and centimeter-sized biotite crystals are present. Furthermore, this sample probably contains the most manifold and heterogeneous texture of all samples. Among zones of intergrown calcite, sanidine and nosean (Fig. 3b), domains with coexisting Ca-carbonate and silicate glass exist (Fig. 3c and d). This suggests immiscible, yet unseparated liquids present in melt interstices of a largely crystallized rock.

Bulk major and trace element compositions of carbonate-bearing syenites

LSC major element compositions fall along a mixing trend between a phonolitic end-member and pure calcite (Fig. 4). Using CO_2 as an indicator of calcite abundance is justified because no other carbonates are present besides rare occurrences of rhodochrosite, and the minor CO_2 contents of nosean are negligible to a first order (Liebsch, 1996). Similarly, broadly linear trends are obtained when plotting trace element abundances against CO_2 (e.g. Sr vs CO_2 yields a correlation coefficient of 0·91). Glass and whole-rock compositions for Laacher See phonolite from units MLST and LLST are an excellent match for the phonolitic end-member (Fig. 4). Based on these linear trends,

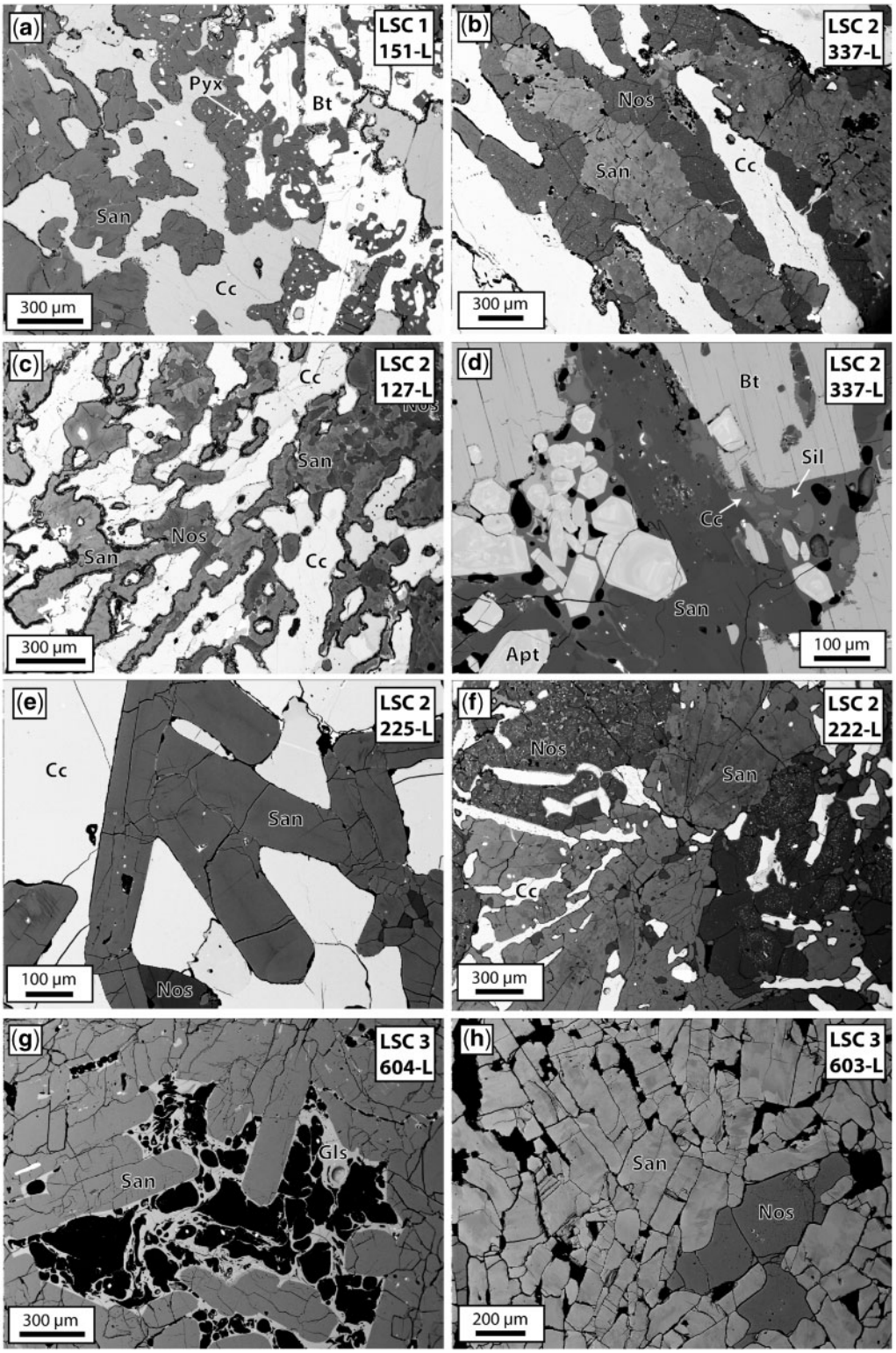

Fig. 3. BSE images of selected carbonatite–syenite samples from Laacher See illustrating the typical and highly variable mineralogical and textural features. (a) 151-L, aegirine–augite pyroxene (Pyx)- and biotite (Bt)-rich domains surrounding sövite droplets, typical for Group 1 (sövite outside field of view). (b, c) 337-L and 127-L, elongated, sinuously intergrown, equigranular calcite (Cc), sanidine (San), and nosean (Nos) crystals interpreted as a eutectic growth texture. (d) 337-L, euhedral apatite (Apt) cumulate showing oscillatory and patchy zoning, probably derived from REE variations. Cc droplets are enclosed in an unknown silicate phase (Sil) and glass. (e) 225-L, euhedral Cc and San indicating co-precipitation. (f) 222-L, San sheaves (fans) intergrown with platy Cc. Inclusion-rich Nos is an early phase containing San, Cc and glass (g) 604-L, sheet-forming San mantled with vesicular glass (Gls). (h) 603-L, San–Nos cumulate typical for Group 3. Black areas in all images are vugs.

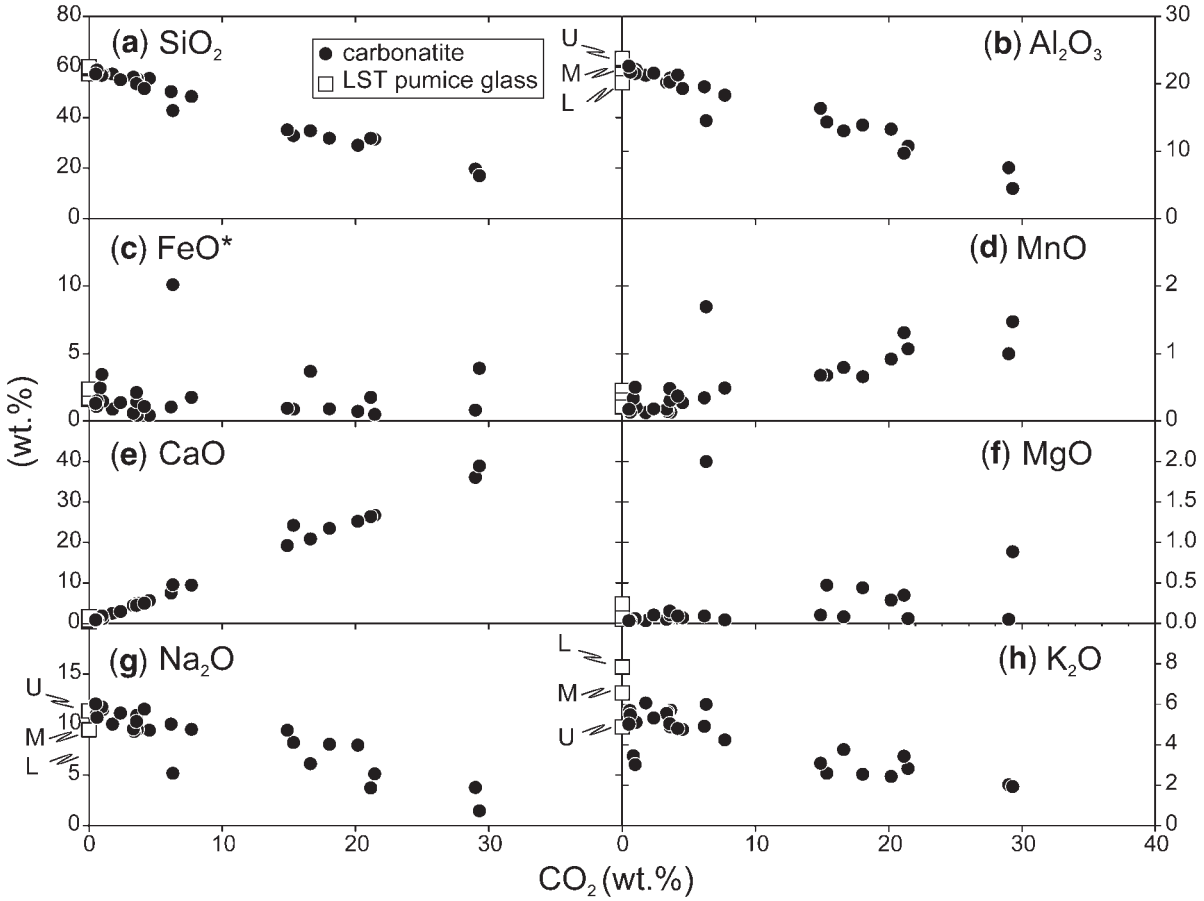

Fig. 4. Major element compositions vs CO_2 (wt %). CO_2 is considered to represent calcite because it is the only CO_2-bearing component (except for the sporadic occurrence of cancrinite and rhodochrosite). FeO is given as total Fe (FeO*). Laacher See Tephra (LST) glass compositions (L, M, U) from Harms & Schmincke (2000).

syenitic carbonatites and carbonate-bearing syenites are composed of only two compositionally distinct components (carbonate and syenite), and the carbonate-rich end-member contains at least ~60 wt % calcite.

Laacher See phonolites have prominent negative Eu anomalies (Eu/Eu* for LLST 1002 = 0·46; for MLST 1034 = 0·72), which also characterize LSC whole-rock compositions (Liebsch, 1996). This is in contrast to other carbonatites in the Eifel volcanic area (e.g. Eu/Eu* for Rieden 727-R = 0·93) that lack significant negative Eu anomalies (Liebsch, 1996). Notably, prominent negative Eu anomalies also occur in LSC accessory phases such as zircon (see below). This is strong evidence for a close genetic link between LSC and differentiated phonolite, which developed prominent negative Eu anomalies as a result of protracted plagioclase fractionation in the phonolite magma (Wörner *et al.*, 1983) prior to carbonatite unmixing and zircon crystallization. Zircon saturation was reached late in the differentiation processes after significant fractionation of mostly feldspars, which is consistent with high Zr concentrations in evolved Laacher See phonolites (1200–2400 ppm Zr; Wörner *et al.*, 1983) necessary for zircon saturation in alkali melts (Watson, 1979; Watson & Harrison, 1983).

Alkali feldspar zonation textures and compositions

Variations in Or and Ab content in alkali feldspars from the carbonate-bearing syenites and silicate cumulate rocks (Tait *et al.*, 1989) are remarkably subtle, and can be visualized only with full contrast in BSE images on the electron microprobe (Fig. 5). Alkali feldspars are characterized by low An contents (<2 mol %), the occurrence of perthitic exsolution domains composed of Ab- and Or-rich lamellae, and a general absence of zoning. The variable density of exsolution lamellae mimics former growth zonation patterns; a particularly well-developed example is shown in Fig. 5c.

These findings contrast with those of Ginibre *et al.* (2004), who described different types of sanidine zonation from Laacher See phonolite phenocrysts. Oscillatory zoned and resorbed or patchy-zoned sanidine occurs within the ULST and MLST pumice. Both such

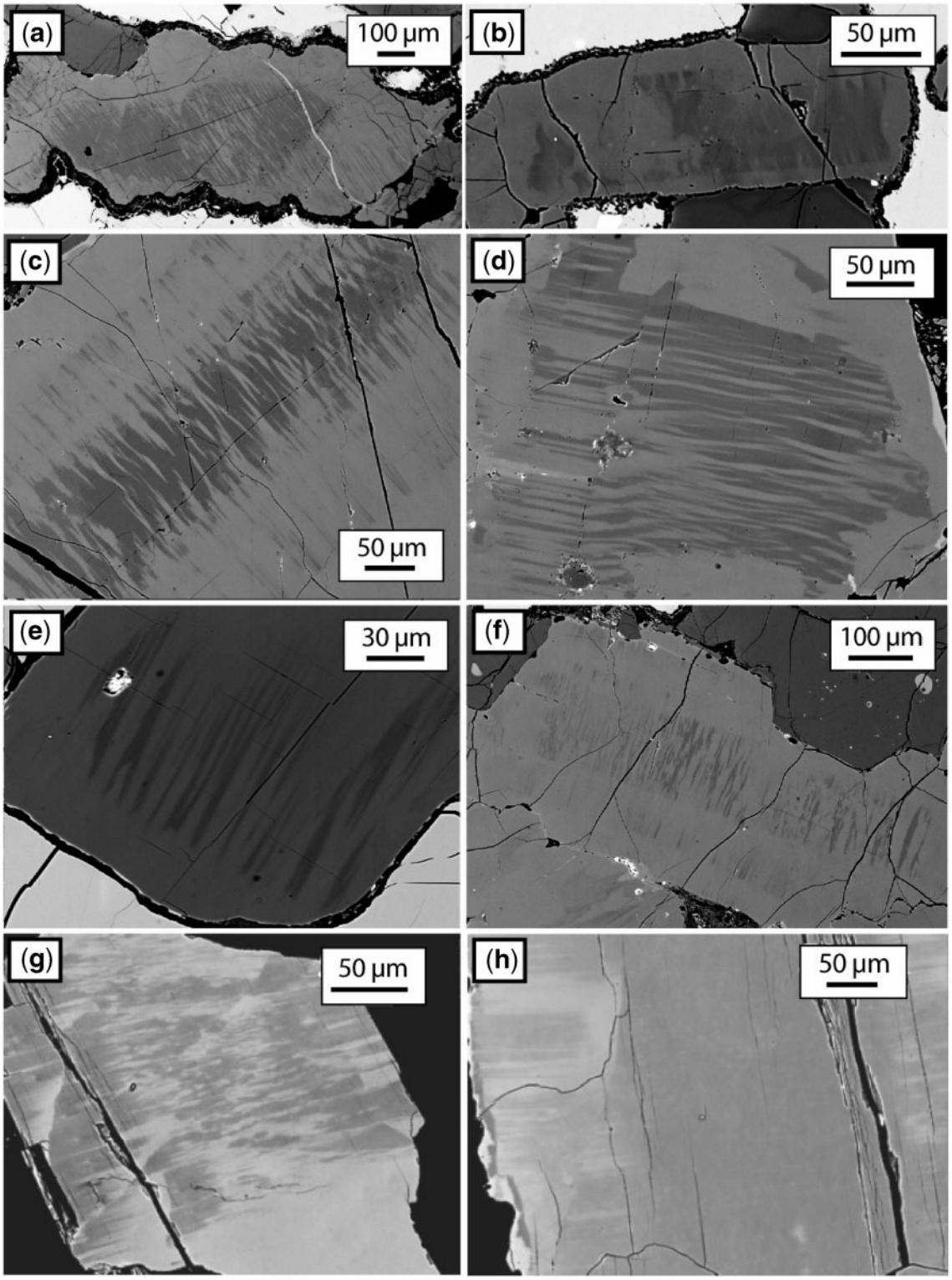

Fig. 5. Sanidine textures observed with EMP BSE imaging. Dark grey colors indicate albite-rich and light grey colors orthoclase-rich domains. The same types of texture have been found in sanidines from LLST and cumulates (g, h) (Ginibre *et al.*, 2004). (a) 127-L, sanidine 2; (b) 222-L, sanidine 7; (c) 523-L, sanidine 5; (d) 337-L, sanidine 5; (e) 225-L, sanidine 1; (f) 523-L, sanidine 1; (g) 1002, high-anorthite patchy composite-type sanidine; (h) 1002, albite-rich core and lamellar outer zone (low-anorthite type).

zonation types, however, are absent in the most evolved phonolitic pumice, which instead shows large textural variations. Some 'composite' crystals are composed of two distinct phases, sanidine and albite, forming intergrown lamellae. These, however, are distinct from the patterned exsolution lamellae described here for the carbonatite syenites. Smooth or patchy zoning patterns that are typical for phenocrystic feldspars from the main body of the Laacher See phonolite (MLST and ULST) are conspicuously absent in the cumulates and carbonate-bearing syenites (Wörner & Schmincke, 1984*a*; Ginibre *et al.*, 2004). Cumulate-type alkali feldspar textures (Tait *et al.*, 1989), however, occur in LLST pumice that represents the uppermost part of the magma chamber (Ginibre *et al.*, 2004). The presence of syenitic feldspars in the most evolved phonolite is a strong indication that the early erupted and shallow phenocryst-poor portion of the Laacher See magma body was contaminated by antecrysts from the plutonic carapace represented by the crystal-rich cumulates (Bourdon *et al.*, 1994; Schmitt, 2006).

Compared with common alkali feldspars, Laacher See carbonatite alkali feldspars have unusually low Ba and Sr contents (see Supplementary Data). Out of more than 625 analyses, fewer than 3% yielded Ba concentrations >1000 ppm, and fewer than 6% yielded Sr concentrations >500 ppm. The majority of Ba and Sr contents fall below the detection limit (<350–300 ppm). Maximum detected concentrations were ~1800 ppm for Ba and ~900 ppm for Sr. In contrast, Ginibre *et al.* (2004) recorded alkali feldspar Ba and Sr concentrations for pumices from an evolved Laacher See phonolite up to 1·6 wt % and 0·4 wt %. Only low-An sanidines from the most differentiated LLST phonolites, however, show Ba and Sr concentrations below the detection limit. These agree well with observed low Sr and Ba concentrations in both carbonatite sanidines and glasses, providing further evidence of a genetic link between the syenite–carbonatite rocks and the most evolved phonolites (see Supplementary Data).

Accessory phases

Zircon, apatite and pyrochlore are ubiquitous accessory minerals in the Laacher See carbonatites. Apatite crystals are commonly anhedral to subhedral and <200 μm. Sample 337-L contains significant amounts of apatite (~2 vol. %) often forming aggregates of subhedral to euhedral grains (Fig. 3d). Zircon crystals are anhedral to euhedral and vary in grain size from tens of micrometers to ~500 μm. CL textures range from oscillatory to patchy zonation, and are described in detail below. Pyrochlore forms yellow–brownish subhedral to euhedral crystals from tens of micrometers to ~300 μm in size. BSE textures range from mostly homogeneous cores to oscillatory zoned rims. Polarized light microscopy and combined energy-dispersive spectrometry (EDX) and BSE imaging also revealed the rare presence of titanite and baddeleyite, which have previously not been described from the carbonatite–syenites. Titanite is mostly anhedral and be up to 250 μm in size, whereas baddeleyite grains are minute (few tens of micrometers).

Zircon textures and trace element compositions

Zircon in the Laacher See carbonatites falls into two categories based on CL textures: (1) regular oscillatory or sector zoning in which CL-distinct bands are oriented along crystallographic features; (2) irregularly zoned zircon with a mottled to swirled intergrowth between CL-dark and CL-bright domains, frequently associated with abundant mineral inclusions. These textures can occur within the same crystals, and there is no regularity with regard to these textures occurring predominantly in crystal interiors or rims. The oscillatory zoned zircon type is more prevalent in Group 3 carbonatites (LSC-3), but both CL zircon types are present in all petrographic groups. Inclusions in zircon include major phases such as sanidine and calcite, as well as occasional Th-rich mineral inclusions (tentatively identified as thorite) that were detected as bright domains in BSE and secondary ion imaging in irregularly zoned zircon domains. These are also abundant in syenitic ejecta from Laacher See and LLST zircon (Schmitt, 2006).

The interpretation of CL maps is aided by SIMS elemental mapping of selected zircon domains. In general, we find that high Th abundances (as estimated from $^{232}ThO_2^-$ normalized to Zr_2O^- to account for secondary ionization variability in the sputtered region) correlate with CL-dark domains (Fig. 6a–c). Ion mapping also shows that Th and Yb abundances are generally correlated. Irregular, CL-bright (and Yb- and Th-poor) patches cross-cut oscillatory growth zones (Fig. 6b and c), which suggests dissolution of igneous zircon and reprecipitation of trace-element-poor zircon, possibly from late-stage melts or fluids that were depleted in high field strength trace elements such as Yb or Th as a result of scavenging of these elements by accessory mineral crystallization.

Zircon REE patterns are HREE-enriched with prominent positive Ce anomalies (Ce/Ce* between ~10 and 100; Fig. 7). Negative Eu anomalies (Eu/Eu* between ~0·3 and 0·7) in zircon correspond to anomalies in the whole-rocks (Fig. 7). By contrast, carbonatitic zircon from other locations (Belousova *et al.*, 2002), as well as those of Rieden (Fig. 7), lack negative Eu anomalies, consistent with the absence of Eu anomalies in the parent Reiden leucite-phonolites. Thus, carbonatitic zircon appears to be a reliable indicator for the REE characteristics of the parental magma.

Hafnon ($HfSiO_4$) and thorite ($ThSiO_4$) components in the Laacher See carbonatite zircon were estimated from HfO_2 and Th abundances from SIMS spot analyses, and are ~0·5–1·5 and <2 mol %, respectively. Higher apparent thorite abundances are possibly caused by beam overlap

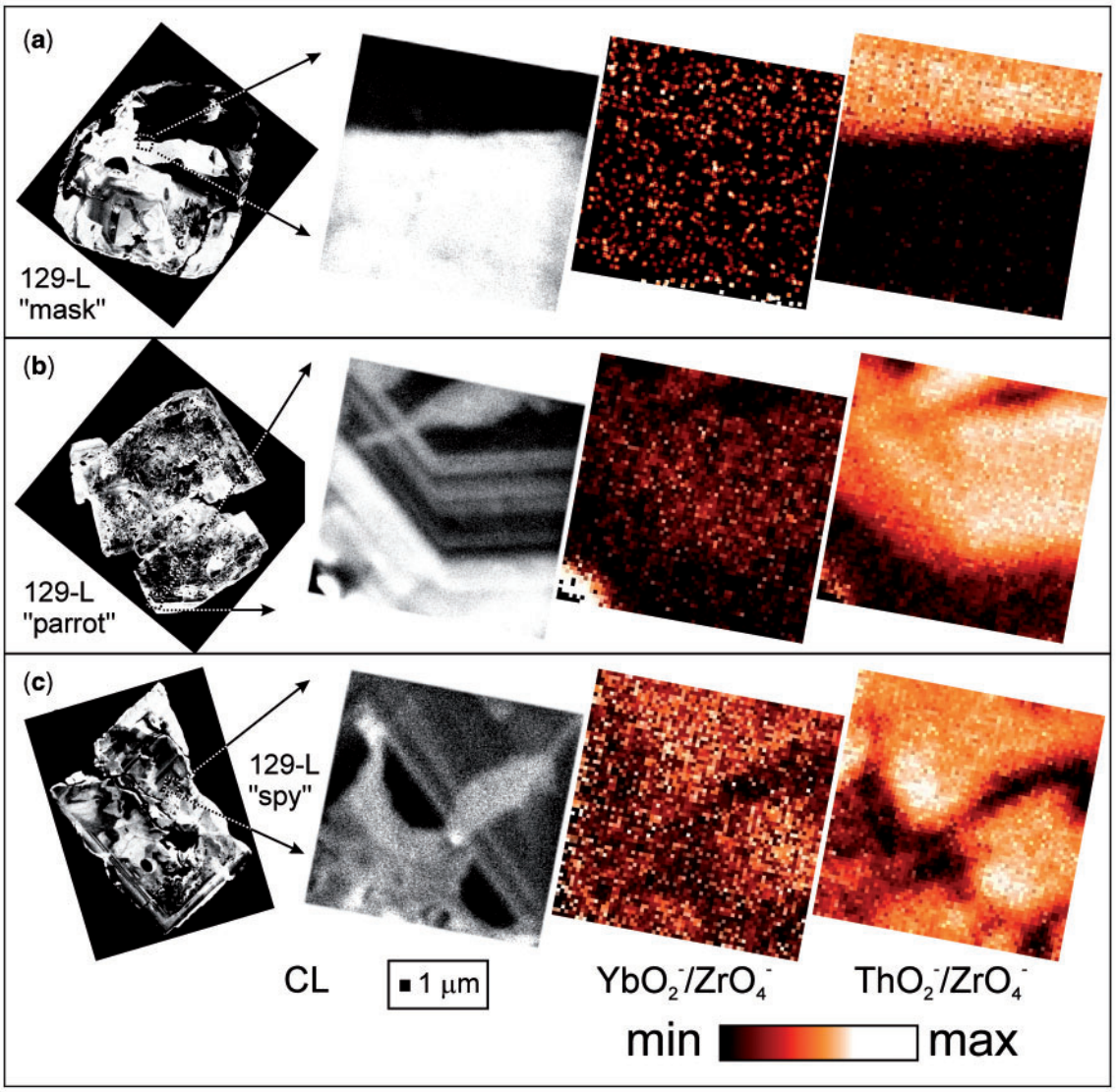

Fig. 6. Selected cathodoluminescence images of zircon crystals from Laacher See carbonatites with high-sensitivity Th and Yb secondary ion maps.

onto small (a few micrometers) inclusions of thorite. Xenotime (YPO_4) substitution is negligible, as evidenced by low (<200 ppm) P abundances. Ti abundances vary between ~2 and 28 ppm. Activities of SiO_2 ($aSiO_2$) and TiO_2 ($aTiO_2$) in the carbonatite magma are low, as indicated by the presence of nosean and baddeleyite, and the lack of Ti-rich minerals (absence of ilmenite and rutile), respectively. In the absence of better constraints, we consider sub-unity activities for SiO_2 and TiO_2 to be compensatory (Ferry & Watson, 2007). This is a reasonable assumption because the reaction

$$\text{baddeleyite}\,(ZrO_2) + SiO_2 = \text{zircon}\,(ZrSiO_4)$$

at 700°C yields $aSiO_2 = 0{\cdot}23$, whereas typical LSC titanomagnetite compositions (e.g. magnetite = 0·88 mol % and ulvöspinel = 0·12 mol %; average of sample 151-L; Liebsch, 1996) and oxygen fugacities at NNO (nickel–nickel oxide buffer; Berndt *et al.*, 2001) indicate $aTiO_2 = 0{\cdot}18$ for the exchange reaction

$$3\,\text{rutile}\,(TiO_2) + 2\,\text{magnetite}\,(Fe_3O_4) = 3\,\text{ulvöspinel}\,(TiFe_2O_4) + O_2$$

with activities calculated using an internally consistent thermodynamic dataset (Holland & Powell, 1998). For $aTiO_2 = aSiO_2$, model Ti-in-zircon temperatures thus range between 567 and 853°C, with an average of 655 ± 58°C (1 standard deviation; $n = 112$). These temperature estimates would be minimum values if Ti partitioning into zircon increases with pressure because of the lower

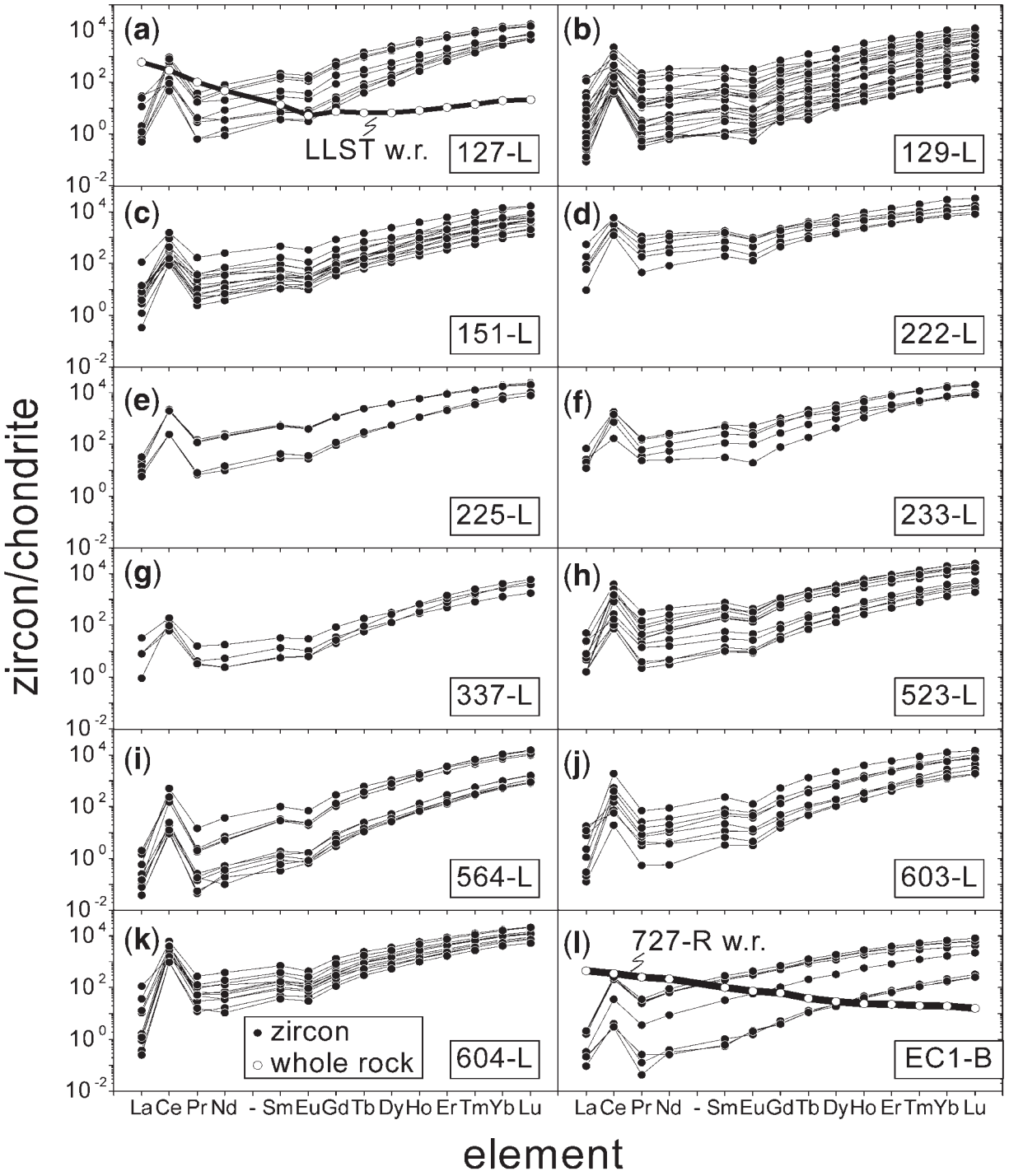

Fig. 7. Chondrite-normalized REE pattern for carbonatite–syenite zircons. Zircons show typical enrichment in HREE relative to whole-rock (w.r.) analyses of phonolite (LLST, Laacher See) and leucite-phonolite (Rieden 727-R). A relatively steady increase from La to Lu is disrupted by prominent positive Ce and negative Eu anomalies. Noteworthy features are the lack of characteristic negative Eu anomaly in older Rieden carbonatite zircon, and negative Eu anomalies in Laacher See carbonatite–syenite zircon, inherited from their respective parental magmas. All chondrite values used in this study are from McDonough & Sun (1995).

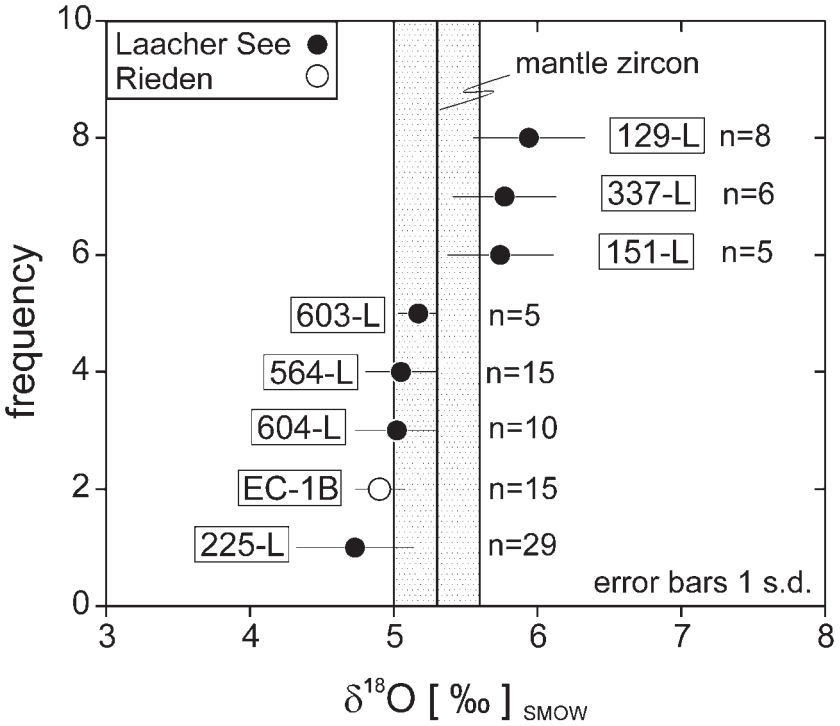

Fig. 8. Zircon oxygen isotopic compositions of Laacher See and Rieden carbonatites in comparison with typical mantle zircon values from Valley (2003). Uncertainties are plotted as 1 standard deviation of *n* replicate analyses.

pressures in the Laacher See magma system relative to the experimental calibration (Ferry & Watson, 2007).

Zircon oxygen isotopes

Average zircon $\delta^{18}O$ (SMOW) values range between 4·7 and 5·9‰; uncertainties estimated from secondary standards are conservatively estimated at ± 0·5‰ (Table 3; Fig. 8; see Supplementary Data). Oxygen isotope compositions are homogeneous on a sample scale, and all values overlap with the range of mantle zircon of 5·3 ± 0·3‰ (Valley, 2003). Zircon $\delta^{18}O$ of all carbonatite samples is invariant with regard to petrographic type or age.

As a result of the slow diffusion of oxygen in zircon (Cherniak & Watson, 2003) and its chemical stability, zircon is largely inert against hydrothermal alteration. This is in contrast to Laacher See bulk carbonate $\delta^{18}O$ values, which vary widely, ranging in $\delta^{18}O$ between 7·9 and 15·9‰ (Liebsch, 1996). The invariant $\delta^{18}O$ in zircon demonstrates that highly variable bulk $\delta^{18}O$ carbonatite compositions were originally close to mantle values, but became subsequently overprinted. With this caveat, a calcite–zircon oxygen isotopic exchange temperatures is calculated using the lowest calcite $\delta^{18}O$ value and isotopic fractionation coefficients complied by Valley (2003), which yields 690 ± 100°C for sample 151-La (calcite $\delta^{18}O = 8·2$‰; zircon $\delta^{18}O = 5·7$‰), close to the average Ti-in-zircon thermometry result (655°C). Despite large uncertainties in both model temperatures, the agreement between methods suggests that the carbonatites formed and resided at temperatures <700°C, the lower bound of estimates for the zoned Laacher See phonolite (720–860°C; Berndt *et al.*, 2001).

Laacher See phonolite melt compositions of $\delta^{18}O = +7·9$‰ are estimated from sanidine analyses, consistent with the elevated $^{87}Sr/^{86}Sr$ ratios of ~0·705 relative to depleted mantle values (Wörner *et al.*, 1985, 1987). Fractionation models predict melt oxygen isotopic compositions that are ~2‰ higher than those of zircon (Trail *et al.*, 2009). Based on carbonatite zircon compositions, the predicted $\delta^{18}O$ for the coexisting syenite melt is between ~6·9 and ~8·1‰, closely overlapping with the phonolite melt values (Wörner *et al.*, 1987). Oxygen isotopes thus also support consanguinity between Laacher See carbonatites and phonolites.

Geochronology

Whole-rock uranium series

Apart from the U–Th whole-rock compositions for Laacher See carbonatites presented here (Table 4), only a few other studies have reported U-series isotope data for carbonatites (Oldoinyo Lengai volcano in the East African Rift; Williams *et al.*, 1986; Pyle *et al.*, 1991).

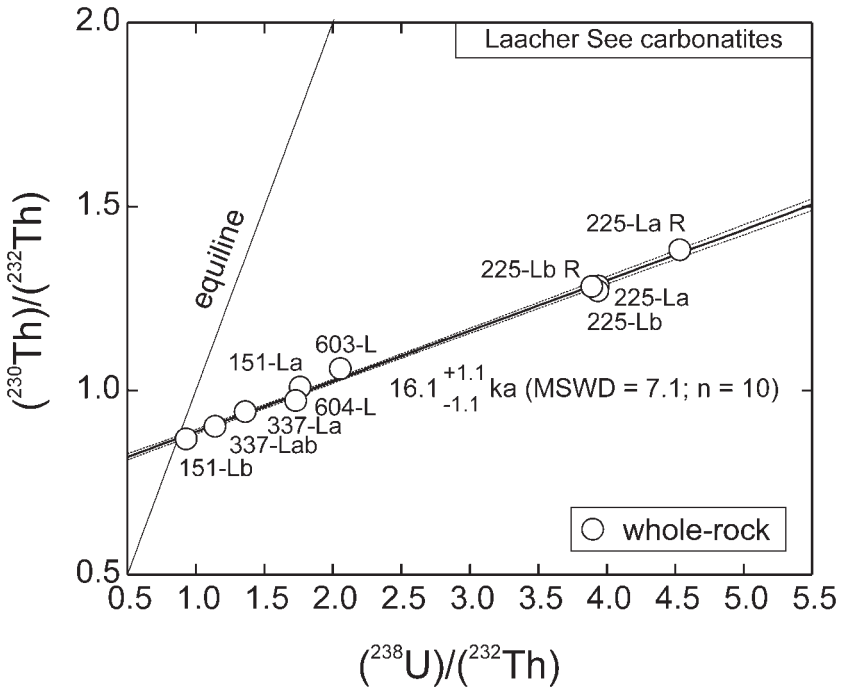

Fig. 9. (^{230}Th)/(^{232}Th) vs (^{238}U)/(^{232}Th) isochron obtained for Laacher See carbonatite whole-rock samples. Whole-rock isochrons are rare (Condomines *et al.*, 2003), and the ~16 ka isochron suggests a major differentiation event that occurred a few thousand years before the eruption, overlapping with the Laacher See phonolite bulk glass separate isochron age of 13·7 +6·7/–6·3 ka [MSWD = 0·41; recalculated from Bourdon *et al.* (1994), using decay constants of Cheng *et al.* (2000)].

Overall, the Laacher See carbonatites have near-unity (^{234}U)/(^{238}U) ratios, with the exception of sample 151-Lb, which is elevated in (^{234}U)/(^{238}U) by 40‰. By contrast, all (^{230}Th)/(^{238}U) ratios for Laacher See carbonatites strongly differ from equilibrium. In the (^{230}Th)/(^{232}Th) vs (^{238}U)/(^{232}Th) diagram, Laacher See carbonatites fall to the right of the equiline, where they define a scattered ~16 ka isochron (Fig. 9; MSWD = 7·1). Sample pairs 225-La and 225-Lb have the highest U abundances of all analyzed Laacher See carbonatites, and were analyzed in replicate. Results for 225-La and its replicate are significantly different (Table 4), yet all analyzed splits of sample 225-L fall on a single isochron. The presence of actinide-rich accessory mineral grains in the rock powders ('nugget effect') probably caused the differences between replicate analyses of 225-La. Two plutonic carbonatite samples from the older Rieden Complex are close to equilibrium (Table 4), with minor excess in ^{230}Th that can be explained by moderately elevated (^{234}U)/(^{238}U). The (^{230}Th)/(^{238}U) equilibrium is consistent with the older age of the Rieden carbonatites.

Zircon uranium-series ages

The accuracy of SIMS U–Th zircon dating was verified by analyzing zircon from a Quaternary Puy de Dôme lava (Fig. 10) previously dated by bulk U–Th analysis (zircon separate provided by M. Condomines). In addition to secular equilibrium zircon AS 3, we also included a carbonatite sample (EC1-B) from the Rieden Complex (Fig. 11) that has a sufficiently old eruption age to be in secular equilibrium, as confirmed by our average ^{206}Pb/^{238}U zircon age of 407 ± 44 ka [n = 8; mean square of weighted deviates (MSWD) = 0·12; see Supplementary Data]. For Puy de Dôme, the bulk TIMS/α-spectrometry zircon–groundmass isochron age (12·7 ± 1·6 ka; 2σ error; Condomines, 1997) agrees well with the corresponding SIMS average age (14·8 ± 2·4 ka; 2σ error; Fig. 10) weighted for U concentration in zircon. For Rieden carbonatite sample EC-1B, the isochron slope (0·89 ± 0·13; MSWD = 1·5; n = 5) overlaps at 95% confidence with the near secular equilibrium slope of ~0·98 expected from U–Pb zircon dating (Table 2; Fig. 11).

U and Th abundances in LSC zircon range widely between <10 ppm and several weight per cent (Table 1). Rare cases with extremely high abundances in Th (>2 wt %) are probably due to beam overlap onto thorite inclusions. Th/U ratios are highly variable, even within zircon from the same sample, and range from ~0·2 to ~700. Laacher See carbonatite zircon exceeds typical igneous zircon Th/U (~0·5), but high Th/U values are characteristic for carbonatitic zircon (Hoskin & Schaltegger, 2003). The intra-sample and intra-grain variability in zircon

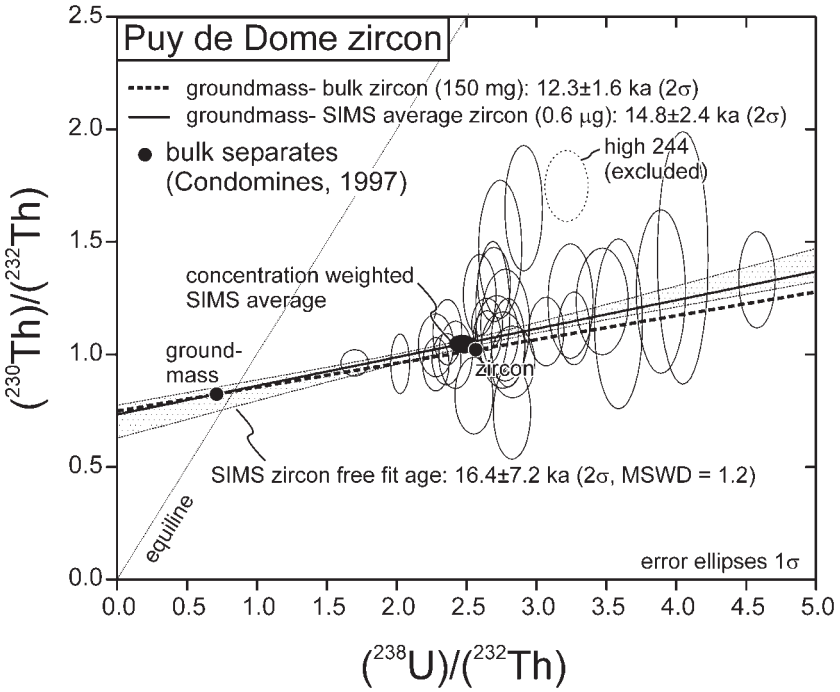

Fig. 10. U–Th isochron diagram for reference zircon from the Puy de Dôme. Bulk U–Th and concentration-weighted average SIMS results agree within uncertainties. It should be noted that the mass of zircon analyzed by SIMS is $\sim 10^5$ times less than that used for bulk analysis by Condomines (1997).

Th/U allows relatively precise U–Th zircon isochrons to be calculated from multiple spots on different crystals, or even within a single crystal (Lowenstern *et al.*, 2000).

Carbonatite clasts 127-L, 222-L, 233-L, and 604-L yield U–Th zircon isochron ages that are indistinguishable from the eruption age, but age uncertainties are permissive of zircon crystallization predating the eruption by several thousand years (Fig. 11). U–Th isochron ages in samples 151-L, 225-L, 337-L, 523-L, 564-L, and 603-L broadly overlap within uncertainties with the previous age group (127-L, 222-L, 233-L, and 604-L), but zircon ages are significantly older than the eruption age (Fig. 11). Sample 129-L stands out by yielding the oldest U–Th zircon isochron age among dated Laacher See carbonatites ($32{\cdot}6 \pm 4{\cdot}1$ ka; MSWD $= 1{\cdot}7$; $n = 24$). For most samples, MSWD values associated with the linear regression are near unity, suggesting that the timescales of zircon crystallization are within analytical uncertainty. For some samples (129-L, 151-L, 222-L), MSWD values are slightly elevated (between 1·7 and 2·0). This could reflect minor zircon age heterogeneity in these samples, or unrecognized analytical uncertainties, potentially as a result of excess counts on $^{230}ThO^+$ that could be caused by primary beam overlap onto calcite inclusions. Regardless of the cause of this minor excess scatter, it was accounted for by multiplying the age uncertainties by the square root of the MSWD when it was significantly >1. We find no correlation between the petrographic groups and their zircon ages. This indicates that the large petrographic and compositional variability is due to local conditions of differentiation and crystallization rather than representing distinct portions of the carapace with different history and age.

Laacher See carbonatite whole-rock Th/U ratios are on average lower than those of zircon. Consequently, whole-rock $(^{238}U)/(^{232}Th)$ plots generally to the right of the centroid of the zircon regression (Fig. 11), although some zircon crystals show 'normal' lower Th/U in zircon relative to silicic melt (Blundy & Wood, 2003). Unusually high Th/U zircon is also present in plutonic xenoliths from Veniaminof volcano (Alaska) that crystallized under near-solidus conditions in the presence of aqueous fluids (Bacon *et al.*, 2007). We tentatively invoke U depletion in the melt as a result of concomitant pyrochlore fractionation and/or decreasing zircon–melt partitioning of U caused by increasing oxidation of U^{4+} to U^{5+} or U^{6+} (Bacon *et al.*, 2007). Regardless of the causes for strong Th/U zircon–carbonatite fractionation, whole-rock $(^{238}U)/(^{232}Th)$ and $(^{230}Th)/(^{232}Th)$ compositions generally fall within the uncertainty bands of the zircon isochrons, indicating isochronous relations between zircon and host carbonatitic syenite melt (as represented by the whole-rock compositions; Table 4).

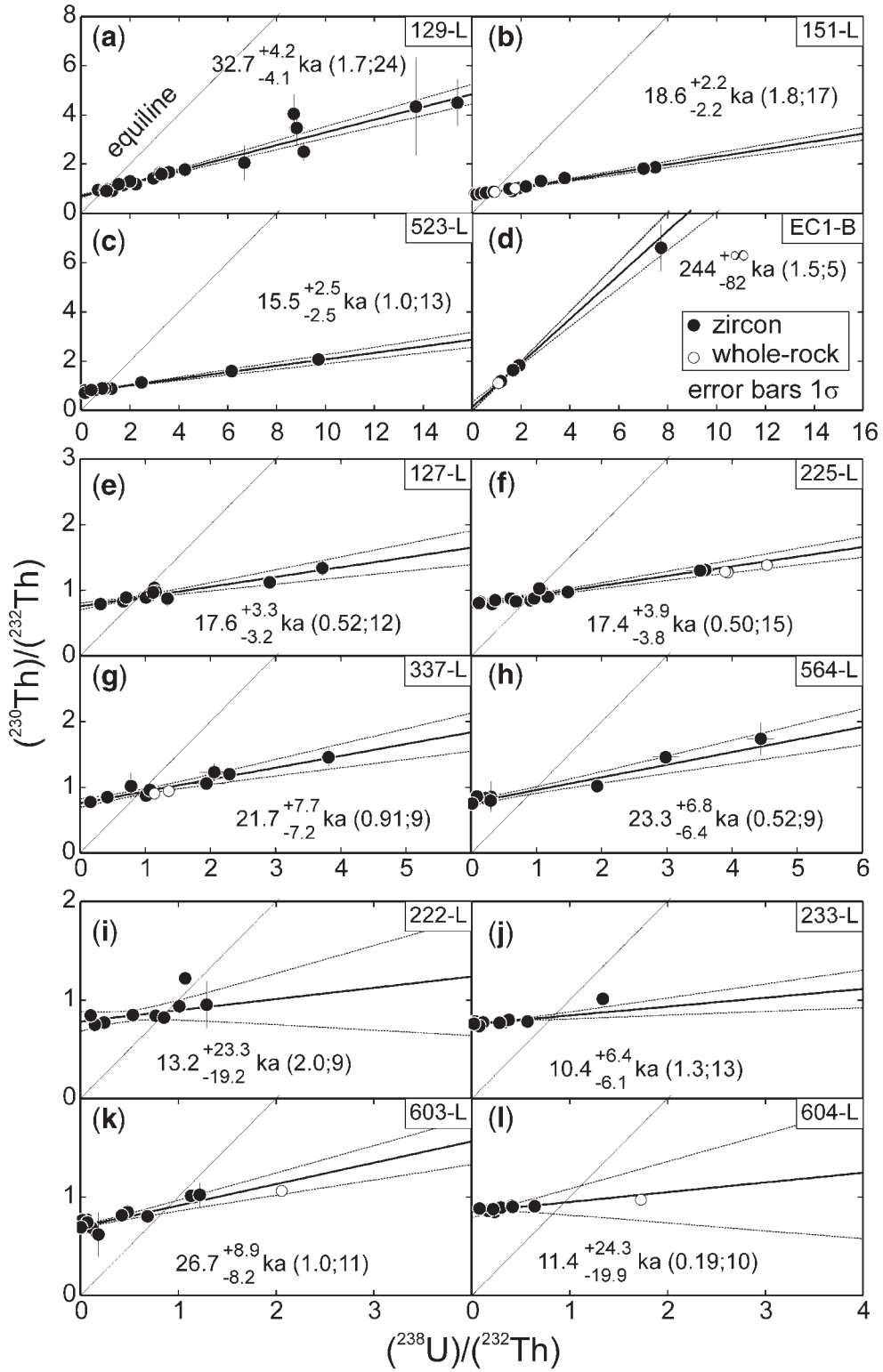

Fig. 11. Zircon U–Th disequilibrium dating results from Laacher See carbonatites with Rieden carbonatite EC1-B shown for comparison. Error bars are plotted as 1σ for clarity, but age uncertainties are given as 2σ; numbers in parentheses indicate MSWD and the number of zircon analyses used for the regression. Equiline is indicated (fine continuous line), and the zircon regression isochron (bold continuous line) with its 95% confidence envelope (dashed lines).

DISCUSSION: NEW INSIGHTS INTO MAGMA EVOLUTION AND STORAGE FROM LAACHER SEE CARBONATITE–SYENITES

Comparison with previous geochronological constraints

The occurrence of evolved phonolite magma that significantly predated the Laacher See eruption was first documented by U-series dating of intermediate to evolved crystal cumulates (Bourdon *et al.*, 1994). Felsic to intermediate cumulate rocks yielded U–Th isochron ages for bulk mineral and glass separates between $29+19/-16$ ka (sample GT828; $n=4$; MSWD = 91) and near-eruption (e.g. B12/13-1; $10+16/-14$ ka; $n=3$; MSWD = 92), whereas the isochron age for mafic cumulate 15592 is $127+\infty/-75$ ka ($n=2$) [all ages were recalculated from Bourdon *et al.* (1994), using Cheng *et al.* (2000) decay constants and scaling uncertainties by the square-root of the MSWD to account for non-analytical scatter, in the same way as we treated our zircon data]. Some of the published ages are based only on two-point isochrons and other results scatter considerably. Mixing of younger with older crystals from the magma chamber margin (Ginibre *et al.*, 2004) or the presence of xenocrysts as demonstrated for zircon in LLST pumice by Schmitt (2006) are unlikely explanations for this scatter in the cumulate minerals, and thus protracted crystallization is a possible scenario. In contrast, bulk-crystal and glass isochrons for more phenocryst-rich pumice are generally more tightly constrained and are typically between $13{\cdot}2+3{\cdot}1/-3{\cdot}0$ ka (MLST pumice 1034; $n=3$; MSWD = 1·7) and $15{\cdot}5+5{\cdot}2/-5{\cdot}0$ ka (ULST pumice 1088; $n=5$; MSWD = 9·0; recalculated from Bourdon *et al.*, 1994). The exception is the bulk separate isochron for crystal-poor LLST pumice (1017; $29{\cdot}3+8{\cdot}5/-7.9$ ka; $n=5$; MSWD = 35) which was attributed to re-mixing of older crystals into the evolved phonolite magma (Bourdon *et al.*, 1994).

From *in situ* analysis of zircon, a tightly constrained isochron (129-L; $32{\cdot}7+4{\cdot}2/-4{\cdot}1$ ka; MSWD = 1·7; $n=24$) yields the oldest LSC crystallization age. This age broadly overlaps with older bulk separate isochrons ages of Bourdon *et al.* (1994). The other LSC zircon isochrons range between ~25 ka and near-eruption ages (Table 2). Several samples (151-L, 523-L, and 225-L) yielded very tightly constrained zircon isochrons with 2σ uncertainties of ±2–4 ka. These comparatively precise ages result from a large spread of zircon along the $(^{238}U)/(^{232}Th)$ axis. It could be argued that limited spread in $(^{238}U)/(^{232}Th)$ and resulting larger uncertainties in some of the younger samples are artefacts of sampling bias. Evidence from U-series bulk-rock data, however, supports the interpretation that carbonatite differentiation and crystallization significantly predating the eruption is real.

To test whether the predominance of zircon crystallization at ~4–5 ka prior to eruption is directly coupled with the formation of the carbonatites, we use the $(^{230}Th/^{232}Th)$ evolution plot of Allègre & Condomines (1976). The evolution of radioactive disequilibria of magmas is plotted against time (expressed as $e^{\lambda t}$), yielding model differentiation ages, provided that closed-system conditions prevailed. This assumption is supported by trace element and oxygen isotope data that indicate consanguinity between Laacher See carbonatites and phonolites. Moreover, both LSC and phonolites are insensitive to contamination because of their high levels of incompatible trace elements.

Figure 12 illustrates $(^{230}Th)/(^{232}Th)$ evolution lines for carbonatite whole-rock samples and 1034 phonolite glass, representing the potential parental melt (Liebsch, 1996). Sample 1034 was chosen as a potential parent because its mineral isochron is better constrained than for the more evolved phonolite glasses 1002 and 1017 (Bourdon *et al.*, 1994). Using the compositions of samples 1002 or 1017, however, does not significantly change the results.

Whereas phonolites are characterized by Th excesses [i.e. a decrease in $(^{230}Th)/(^{232}Th)$ with time] the carbonatites display particularly strong U excesses causing $(^{230}Th)/(^{232}Th)$ to increase with time. The intercepts of the carbonatites with the 1034 line yield initial $(^{230}Th)/(^{232}Th)_0$ and the time since carbonatite extraction from phonolite. Based on textural evidence for the presence of carbonatitic droplets enclosed by carbonate-poor syenite (group LSC-1), we favor unmixing of carbonatitic liquid from evolved phonolite at the top of the Laacher See magma chamber; however, the detailed mechanisms of carbonatite melt generation are beyond the scope of this study. In any case, differentiation via liquid immiscibility, fractional crystallization, or a combination thereof, would leave $(^{230}Th)/(^{232}Th)$ between parent and daughter melts unchanged.

LSC differentiation model ages (Table 2; Fig. 12) are summarized in Fig. 13 along with zircon crystallization age probability density curves. The age distribution is truncated by the eruption age because of the impossibility of post-eruption carbonatite differentiation or zircon crystallization. Zircon crystallization ages and carbonatite model differentiation ages both show a similar age peak. This result leaves a remarkably short (within the resolution of U-series dating at a few thousand years) interval between differentiation and zircon crystallization. The average carbonatite formation age ($16{\cdot}7\pm1{\cdot}4$ ka; MSWD = 0·49; $n=10$) clearly predates the eruption, but the situation prior to this dominant differentiation interval is obscure because of the small number of sampled carbonatites that fall into this older age range. Only sample 129-L has a significantly older zircon crystallization age

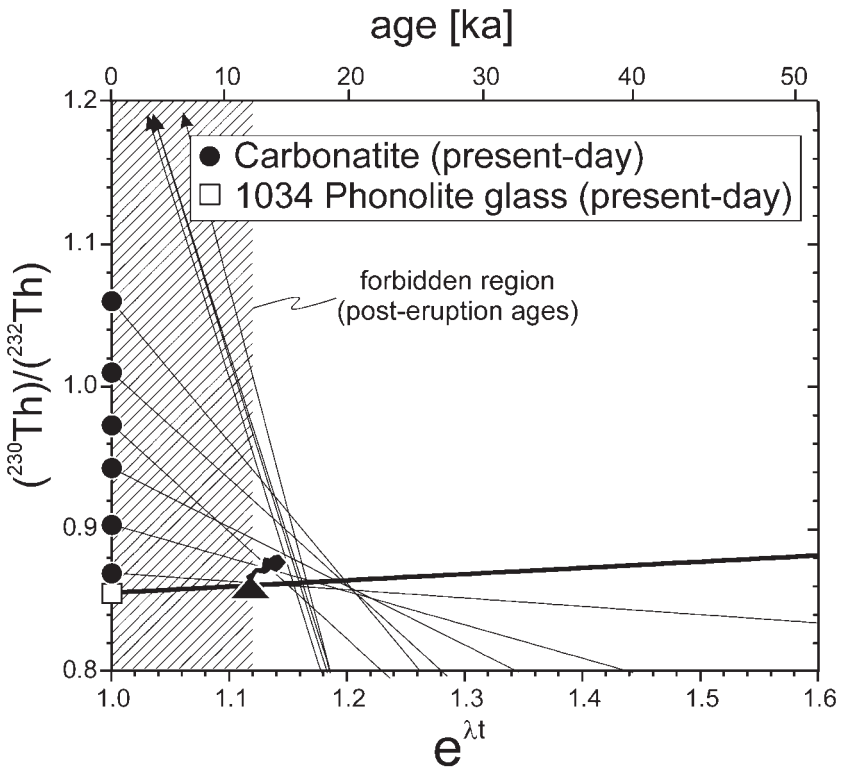

Fig. 12. (^{230}Th/^{232}Th) evolution lines as a function of time ($e^{\lambda t}$). The *y*-axis intercepts represent measured (^{230}Th/^{232}Th). Bold line represents 1034 phonolite as the silicic parent. Carbonatite evolution line intercepts with the evolution line of phonolite sample 1034 mark the time when carbonatite melt last coexisted; that is, was extracted with enriched U/Th, and subsequently developed in a closed system.

of ~33 ka, but whole-rock analysis was impossible because of its small sample size.

U–Th zircon crystallization ages and carbonatite differentiation model ages both support a discrete phase of carbonatite differentiation in the Laacher See magma system. Zircon ages of ~17 ka for LLST (Schmitt, 2006) agree with the age peak for carbonatite differentiation and crystallization. We concur with Bourdon *et al.* (1994) that the LLST crystal ages reflect crystal re-mixing from the plutonic part of the magma system into the crystal-poor phonolite magma during or immediately prior to eruption. ^{40}Ar/^{39}Ar sanidine ages for the LLST dominantly record the age of the eruption, but minor populations of LLST sanidines with ages of ~12 ka and even up to ~115 ka older than the eruption exist (Bogaard, 1995). Because xenocrystic sanidine partially degasses during magmatic storage or volcanic eruption (Spell *et al.*, 2001), the significance of these pre-eruptive sanidine ages as crystallization ages is dubious. We note, however, that the older ages are consistent with zircon evidence for crystal recycling from syenitic intrusive rocks. The 127 ka two-point isochron age (defined by clinopyroxene and apatite) of a mafic cumulate (Bourdon *et al.*, 1994) is without equivalent among the carbonatitic and syenitic ejecta thus far analyzed.

Feldspar textures in support of uranium-series ages

Before discussing the implication of the carbonatite ages for the evolution of the Laacher See magma system, it is instructive to compare the accessory mineral U-series crystallization ages with textural evidence for protracted crystal residence of major phases such as alkali feldspar. The U–Th zircon ages of the carbonatites reflect partial solidification of phonolite-derived differentiated daughter magmas that were generated over a time-span of at least ~10–20 kyr prior to eruption. The residence age of the magma system is supported by a striking concordance of crystal residence inferred from sanidine textures and zircon crystallization ages. The near absence of zonation in most plutonic feldspars, which is in strong contrast to phenocrystic minerals in the liquid-dominated portions of the Laacher See eruptive rocks as represented by pumice clasts, indicates that the carbonatitic syenites resided for a prolonged time at subsolidus temperatures that first allowed for almost complete diffusive homogenization and then the development of exsolution textures, which have never been observed in Laacher See phonolitic phenocrysts. The concordance of residence ages for the Laacher See system suggests that the growth environment, at least

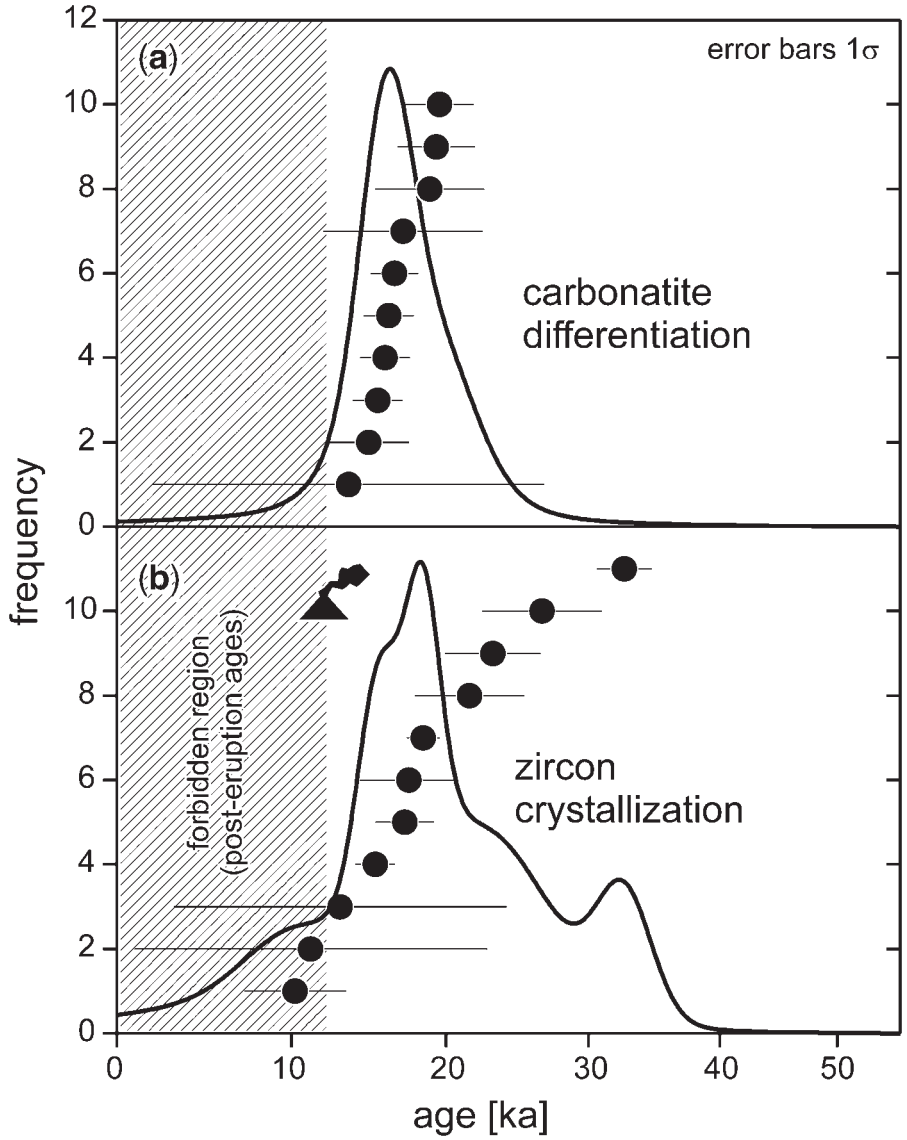

Fig. 13. Relative probability density plots for bulk-rock differentiation ages and zircon crystallization ages. Both functions show major peaks, closely overlapping at ~17 ka. Error bars plotted as 1σ. Shaded area is a forbidden region for differentiation and zircon crystallization based on the $^{40}Ar/^{39}Ar$ sanidine eruption age of 12·90 ± 0·56 ka (Bogaard, 1995). (a) Model carbonatite–silicate differentiation ages from Table 4; (b) zircon isochron ages from Table 2.

on the scale of single plutonic ejecta clasts, was very homogeneous. Crystallization occurred within less than a few thousand years, indicated by the temporal resolution of overlapping U-series differentiation and zircon crystallization ages, with no separation between early sanidine and late zircon. Subsequent subsolidus storage at temperatures <700°C favored sanidine equilibration and exsolution. On this basis, it is conceivable that sanidines from samples that yield near-eruption zircon crystallization ages might still be zoned. However, as this is not observed, rapid sanidine equilibration must have occurred during pre-eruptive crystal storage, and was facilitated by crystal residence at elevated temperatures. Therefore, we envisage a carapace of intrusive and cumulate rocks with a core of evolving magma that eventually became compositionally zoned prior to eruption, rather than a plexus of small-volume single intrusions, which would have cooled rapidly and would not have resulted in a common differentiation trend (Fig. 14).

It has often been observed that direct dating by U-series mineral isochrons results in ages that are older than residence times indicated by diffusion modeling of zoned

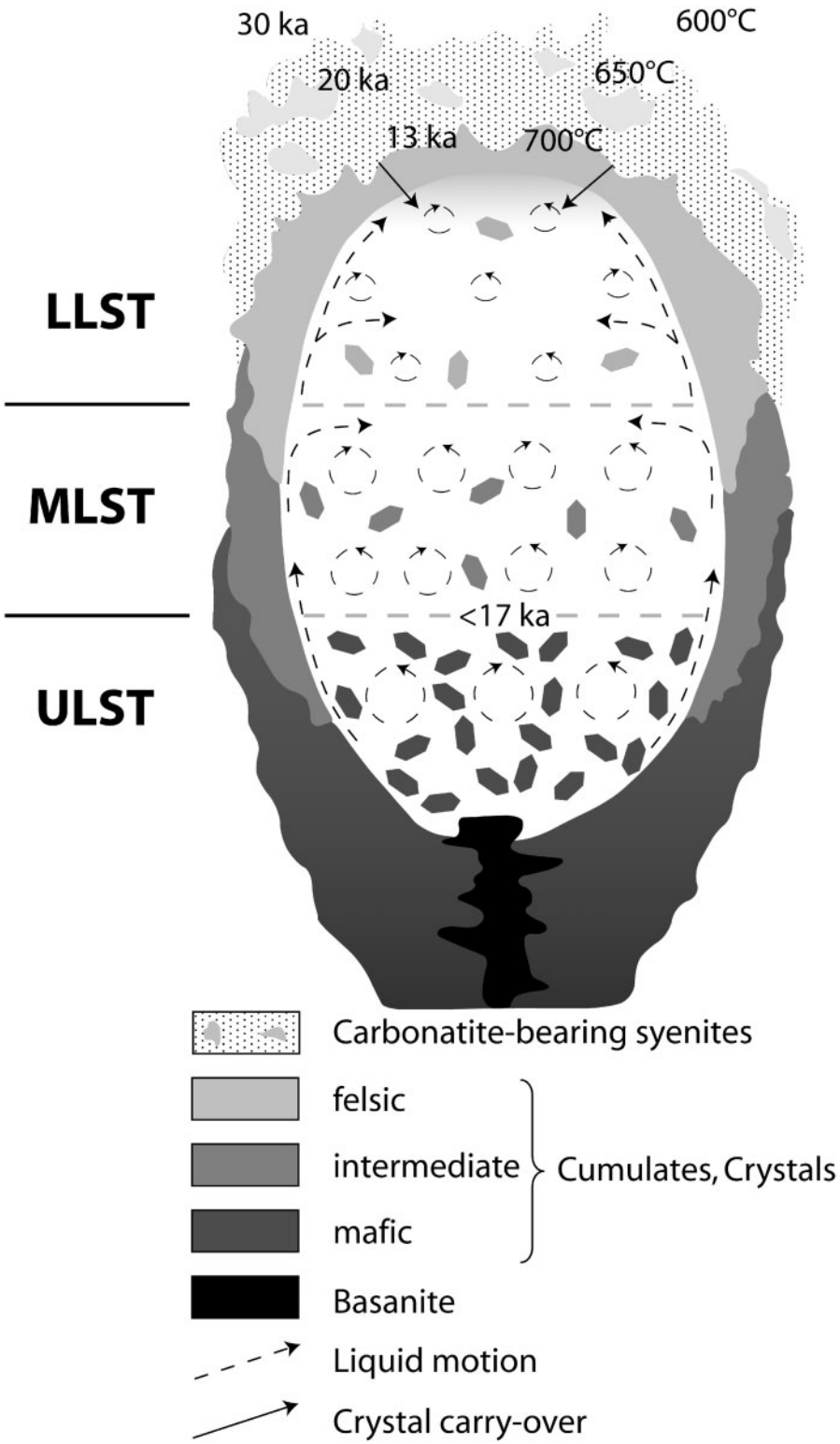

Fig. 14. Schematic reconstruction of the Laacher See magma chamber just prior to eruption (after Wörner & Schmincke, 1984*b*; Tait *et al*., 1989; Ginibre *et al*., 2004). New evidence for prolonged evolution, residence and cooling based on new U-series dating, compositional data and petrographic observations is added to delineate the temporal and thermal evolution of the intrusive syenite–carbonatite complex surrounding the Laacher See magma chamber.

phenocryst minerals (e.g. Zellmer *et al.*, 1999; Hawkesworth *et al.*, 2004; Morgan *et al.*, 2004; Morgan & Blake, 2006). Our results, however, indicate that in the Laacher See case, mineral zonation (or the lack thereof) and U-series dating yield at least qualitatively compatible estimates for crystal residence that was short (within hundreds of years to a few thousand years) for the residual Laacher See phonolite at 720–860°C (Berndt *et al.*, 2001; Ginibre *et al.*, 2004) compared with the age (within thousands to tens of thousand years) of co-genetic plutonic carbonatites at temperatures of <700°C.

The magma chamber prior to eruption

Cogenetic plutonic ejecta have a strong potential to gauge the pulse of magmatic differentiation (Bacon *et al.*, 2007); however, their unknown spatial origins or entrainment mechanisms during eruption obfuscate this geochemical and geochronological record. The Laacher See intrusive carbonatites indicate differentiation and crystallization significantly predating the eruption; however, the age resolution is insufficient to unambiguously distinguish between continuous or episodic evolution of the magma system. The scarcity of early crystallized carbonatites, for example, could result from volumetrically minor carbonatite generation in the early stages of the Laacher See magma chamber as a result of gradual accumulation of a phonolite magma body that is unrelated to earlier intrusions (Schmitt, 2006). However, we cannot expect that the sampling of syenites and cumulates is necessarily representative of the abundance of these rocks in the magma chamber's carapace, and therefore the abundance of rocks with older ages does not relate to their abundance at depth.

We observe a remarkable compositional homogeneity in LSC over time with only small variations in major or trace elements that could be easily attributed to minor fractional crystallization of accessory phases. More importantly, the lack of major and trace element variation in the silicate end-member of different ages suggests that there was no significant variability in composition. This implies that the carbonatite–syenite intrusive complex in the periphery of the Laacher See magma chamber had been fed by essentially the same magma composition since at least ~33 ka. We therefore argue that younger intrusive rocks in close proximity to the eruptible liquid-dominated interior of the magma system are overrepresented in the LSC ejecta population relative to older peripheral domains (Fig. 14).

The formation of the carbonatitic syenites requires cooling from initial magmatic temperatures (>860°C for mafic phonolite to ~720°C for the most evolved phonolite; Berndt *et al.*, 2001) to lower and possibly subsolidus temperatures <700°C indicated by Ti-in-zircon and oxygen isotope thermometry. Nevertheless, parts of the intrusive system must have resided at elevated temperatures because alkali feldspar exsolution is not omnipresent. Exsolution features in feldspar are particularly rare in samples with zircon crystallization ages near the eruption age (233-L, 604-L) implying higher temperatures than in samples with older zircon ages. It is emphasized that this correlation has not been found for all samples. It seems, however, reasonable to assume that samples with younger zircon crystallization ages resided more closely to the hotter magma chamber interior.

The peak in carbonatite ages at ~17 ka (Fig. 13) is only slightly older than MLST and ULST mineral and glass isochron ages of ~13–15 ka (Bourdon *et al.*, 1994). The onset of crystallization in the liquid-dominated portion of the Laacher See chamber thus appears to be almost coeval with the main phase of carbonatite differentiation and crystallization. The older (and more heterogeneous) isochron age for early erupted LLST is not in violation of this scenario because it can be explained by crystal carry-over from older intrusive rocks (Bourdon *et al.*, 1994). Ginibre *et al.* (2004) and Schmitt (2006) presented evidence for both processes from the study of LLST sanidine and zircon crystals, respectively. Carbonatitic ejecta clast 129-L, however, provides evidence that phonolite–carbonatite differentiation had already started ~10–20 kyr earlier. Crystal removal through settling or resorption following reheating of the liquid-dominated domains of the magma system could reconcile disparate crystal age records in intrusive LSC and Laacher See pumice.

Based on these new results, a much better constrained model for the Laacher See magma chamber and its temporal evolution prior to eruption can be established (Fig. 14). Protracted differentiation of phonolite magma is indicated by zircon isochrons for intrusive carbonatites (this study) and mineral and glass separates for cumulates (Bourdon *et al.*, 1994). The temporal resolution of *in situ* crystal dating and bulk methods at millennial time scales is sufficient to reveal crystallization and differentiation episodes at the scale of single ejecta clasts. Differentiation initiated as early as ~33 ka and lasted until the eruption at ~12·9 ka, with a prominent peak around ~17 ka. Because evolved phonolite magmas already existed at ~33 ka contemporaneous with more mafic cumulates of similar age (Bourdon *et al.*, 1994), the system was probably recharging and differentiating at the same time. From ~17 ka onward, the magmatic system may have become increasingly closed and in its core a zoned phonolite magma chamber evolved. This is also consistent with predictions from fluid-dynamic models for time required to generate a zoned phonolite magma chamber with the dimensions of the Laacher See system (Tait *et al.*, 1989), the lack of older crystals (other than antecrysts from the carapace) in the erupted pumice, and the young glass isochron for compositionally zoned LLST, MLST, and ULST pumice (Bourdon *et al.*, 1994). However, mafic recharge and mixing between the zoned phonolite magma body and

a new input of basanite magma directly from the mantle (Wörner & Wright, 1984) provides clear evidence that the Laacher See magma chamber remained active and evolving.

The occurrence of old crystal ages in cognate carbonatitic syenites and felsic cumulates from the Laacher See volcano implies that highly evolved phonolite magma already had formed in significant volumes from prior differentiation of parental basanite magma. This not only places the residence age of the evolved phonolite magma system to at least ~10–20 kyr prior to the eruption with a much higher precision than previously possible, but also implies that phonolite differentiation from a parental basanite must have occurred before that time, the extent of which is unconstrained by our data. The Laacher See volcano erupted within few thousand years after a major magmatic differentiation and zonation event that took place in a relatively long-lived magma system (dating back to at least ~33 ka) that may still be active today.

CONCLUSIONS

(1) The origin of the parental melt that produced the Laacher See carbonatite–syenite suite is a mantle-derived magma that differentiated to phonolite with negligible assimilation.

(2) A strong genetic link exists between highly evolved phonolite from the uppermost part of the magma chamber and the carbonatite–syenite complex, with negligible variation in the composition of the silicate parent magma over the entire differentiation period.

(3) Intrusive syenite–carbonatites form a texturally and compositionally complex subvolcanic association at the magma chamber margins; however, with the exception of older crystals present in LLST pumice, they remained largely decoupled from the main body of compositionally zoned phonolite magma.

(4) U-series zircon crystallization ages refine previous bulk separate isochron ages and reveal that the evolved Laacher See magma system existed and/or accumulated over at least 20 kyr prior to the eruption of the residual phonolite magmas at ~12·9 ka.

(5) Single xenoliths yield tightly constrained zircon crystallization ages, in favourable cases with an ~2–3 kyr resolution (2σ). Zircon crystallization and bulk-rock model differentiation ages overlap and peak at ~4 kyr prior to eruption.

(6) Alkali feldspars in syenite–carbonatite ejecta lack magmatic compositional zoning patterns, and show exsolution textures that result from extended low-T sub-solidus residence. Small compositional and textural differences probably reflect spatial and thermal heterogeneities.

(7) The subvolcanic syenite–carbonatite complex was probably older and cooler at its margin, with a compositionally zoned and hotter phonolite core. A decline in carbonatite differentiation and an entirely young (overlapping within uncertainty with the eruption age) phenocryst population in the main portion of the phonolite magma body could indicate a major reorganization of the Laacher See magma system prior to eruption.

(8) Prolonged residence times for the phonolitic Laacher See magma are in accordance with other medium-sized, evolved alkaline systems (e.g. Vesuvius; Scheibner *et al.*, 2008; Campi Flegreii; Arienzo *et al.*, 2009). Thus it appears that pre-eruptive residence and magmatic evolution times of few thousand to at most a few tens of thousand years are typical for such systems. This is significantly longer than for mafic magmatic evolution but shorter than for large-volume silicic magma reservoirs (Reid *et al.*, 1997; Hawkesworth *et al.*, 2000, 2004; Charlier *et al.*, 2003, 2005; Cooper & Reid, 2008).

ACKNOWLEDGEMENTS

Tracy Howe is thanked for zircon imaging and sample preparation. Andreas Kronz is acknowledged for support with electron microprobe analyses. The manuscript benefited from reviews by Michel Condomines, Charles Bacon, and Bernard Bourdon, and by discussions with H.-U. Schmincke. Michel Condomines is also thanked for providing the Puy de Dôme zircons. This work was supported by the Petrology and Geochemistry Program, Division of Earth Sciences, National Science Foundation (grant number 0838585 to A.K.S.), the Deutsche Forschungsgemeinschaft (DFG) (grant number 362/33-1 to G.W.), and the German Academic Exchange Service (DAAD) (travel grant to F.W.). The ion microprobe facility at UCLA is partly supported by grants from the Instrumentation and Facilities Program, Division of Earth Sciences, National Science Foundation.

SUPPLEMENTARY DATA

Supplementary data for this paper are available at *Journal of Petrology* online.

REFERENCES

Allègre, C. J. & Condomines, M. (1976). Fine chronology of volcanic processes using ^{238}U–^{232}Th systematics. *Earth and Planetary Science Letters* **28**, 395–406.

Arienzo, I., Civetta, L., Heumann, A., Wörner, G. & Orsi, G. (2009). Isotopic evidence for open system processes within the Campanian Ignimbrite (Campi Flegrei—Italy) magma chamber. *Bulletin of Volcanology* **71**, 285–300.

Baales, M., Joris, O., Street, M., Bittmann, F., Weninger, B. & Wiethold, J. (2002). Impact of the late glacial eruption of the Laacher See volcano, Central Rhineland, Germany. *Quaternary Research* **58**, 273–288.

Bacon, C. R., Sisson, T. W. & Mazdab, F. K. (2007). Young cumulate complex beneath Veniaminof caldera, Aleutian arc, dated by zircon in erupted plutonic blocks. *Geology* **35**, 491–494.

Baertschi, P. (1976). Absolute ^{18}O content of Standard Mean Ocean Water. *Earth and Planetary Science Letters* **31**, 341.

Belousova, E. A., Griffin, W. L., O'Reilly, S. Y. & Fisher, N. I. (2002). Igneous zircon; trace element composition as an indicator of source rock type. *Contributions to Mineralogy and Petrology* **143**, 602–622.

Berndt, J., Holtz, F. & Koepke, J. (2001). Experimental constraints on storage conditions in the chemically zoned phonolitic magma chamber of the Laacher See Volcano. *Contributions to Mineralogy and Petrology* **140**, 469–486.

Blundy, J. & Wood, B. (2003). Mineral–melt partitioning of uranium, thorium and their daughters. In: Bourdon, B., Henderson, G., Lundstrom, C. & Turner, S. (eds) *Uranium-Series Geochemistry. Mineralogical Society of America, Reviews in Mineralogy and Geochemistry* **52**, 59–123.

Bogaard, P. J. F. & Wörner, G. (2003). Petrogenesis of basanitic to tholeiitic volcanic rocks from the Miocene Vogelsberg, Central Germany. *Journal of Petrology* **44**, 569–602.

Bogaard, v. d. P. (1995). $^{40}Ar/^{39}Ar$ ages of sanidine phenocrysts from Laacher See tephra (12,900 yr BP); chronostratigraphic and petrological significance. *Earth and Planetary Science Letters* **133**, 163–174.

Bogaard, v. d. P. & Schmincke, H.-U. (1984). The eruptive center of the late Quaternary Laacher See tephra. *Geologische Rundschau* **73**, 933–980.

Bogaard, v. d. P. & Schmincke, H.-U. (1985*a*). Aschenlagen als quartäre Zeitmarken in Mitteleuropa. *Geowissenschaften* **6/3**, 75–84.

Bogaard, v. d. P. & Schmincke, H.-U. (1985*b*). Laacher See Tephra; a widespread isochronous late Quaternary tephra layer in Central and Northern Europe. *Geological Society of America Bulletin* **96**, 1554–1571.

Bogaard, v. d. C., Bogaard, v. d. P. & Schmincke, H.-U. (1989*a*). Quartärgeologisch-tephrostratigraphische Neuaufnahme und Interpretation des Pleistozänprofils Kärlich. *Eiszeitalter und Gegenwart* **39**, 62–86.

Bogaard, v. d. P., Hall, C. M., Schmincke, H.-U. & York, D. (1989*b*). Precise single-grain $^{40}Ar/^{39}Ar$ dating of a cold to warm climate transition in Central Europe. *Nature* **342**, 523–525.

Booth, A. L., Kolodny, Y., Chamberlain, C. P., McWilliams, M., Schmitt, A. K. & Wooden, J. (2005). Oxygen isotopic composition and U–Pb discordance in zircon. *Geochimica et Cosmochimica Acta* **69**, 4895–4905.

Bourdon, B., Zindler, A. & Wörner, G. (1994). Evolution of the Laacher See magma chamber; evidence from SIMS and TIMS measurements of U–Th disequilibria in minerals and glasses. *Earth and Planetary Science Letters* **126**, 75–90.

Brauns, A. & Brauns, R. (1925). Ein Carbonatit aus dem Laacher Seegebiet. *Centralblatt fiir Mineralogie, Geologie und Paläontologie A* **4**, 97–101.

Charlier, B. L. A., Peate, D. W., Wilson, C. J. N., Lowenstern, J. B., Storey, M. & Brown, S. J. A. (2003). Crystallisation ages in coeval silicic magma bodies; ^{238}U–^{230}Th disequilibrium evidence from the Rotoiti and Earthquake Flat eruption deposits, Taupo volcanic zone, New Zealand. *Earth and Planetary Science Letters* **206**, 441–457.

Charlier, B. L. A., Wilson, C. J. N., Lowenstern, J. B., Blake, S., van Calsteren, P. W. & Davidson, J. P. (2005). Magma generation at a large, hyperactive silicic volcano (Taupo, New Zealand) revealed by U–Th and U–Pb systematics in zircons. *Journal of Petrology* **46**, 3–32.

Cheng, H., Edwards, R. L., Hoff, J., Gallup, C. D., Richards, D. A. & Asmerom, Y. (2000). The half-lives of uranium-234 and thorium-230. *Chemical Geology* **169**, 17–33.

Cherniak, D. J. & Watson, E. B. (2003). Diffusion in zircon. In: Hanchar, J. M. & Hoskin, P. W. O. (eds) *Zircon. Mineralogical Society of America, Reviews in Mineralogy and Geochemistry* **53**, 113–143.

Condomines, M. (1997). Dating recent volcanic rocks through Th-230–U-238 disequilibrium in accessory minerals: Example of the Puy de Dôme (French Massif Central). *Geology* **25**, 375–378.

Condomines, M., Tanguy, J. C. & Michaud, V. (1995). Magma dynamics at Mt Etna—constraints from U–Th–Ra–Pb radioactive disequilibria and Sr isotopes in historical lavas. *Earth and Planetary Science Letters* **132**, 25–41.

Condomines, M., Gauthier, P.-J. & Sigmarsson, O. (2003). Timescales of magma chamber processes and dating of young volcanic rocks. In: Bourdon, B., Henderson, G., Lundstrom, C. & Turner, S. (eds) *Uranium-Series Geochemistry. Mineralogical Society of America, Reviews in Mineralogy and Geochemistry* **52**, 125–174.

Cooper, K. M. & Donnelly, C. T. (2008). ^{238}U–^{230}Th–^{226}Ra Disequilibria in dacite and plagioclase from the 2004–2005 eruption of Mount St. Helens. In: Sherrod, D. R., Scott, W. E. & Stauffer, P. H. (eds) *A Volcano Rekindled: The First Year of Renewed Eruption at Mount St. Helens, 2004–2006. US Geological Survey Professional Paper* **1750**, 827–846.

Cooper, K. M. & Reid, M. R. (2008). Uranium-series crystal ages. In: Putirka, K. D. & Tepley, F. J. (eds) *Minerals, Inclusions and Volcanic Processes. Mineralogical Society of America, Reviews in Mineralogy and Geochemistry* **69**, 479–544.

Ferry, J. M. & Watson, E. B. (2007). New thermodynamic models and revised calibrations for the Ti-in-zircon and Zr-in-rutile thermometers. *Contributions to Mineralogy and Petrology* **154**, 429–437.

Ginibre, C., Wörner, G. & Kronz, A. (2004). Structure and dynamics of the Laacher See magma chamber (Eifel, Germany) from major and trace element zoning in sanidine; a cathodoluminescence and electron microprobe study. *Journal of Petrology* **45**, 2197–2223.

Harms, E. & Schmincke, H.-U. (2000). Volatile composition of the phonolitic Laacher See magma (12,9000 yr BP); implications for syn-eruptive degassing of S, F, Cl and H_2. *Contributions to Mineralogy and Petrology* **138**, 84–98.

Harms, E., Gardner, J. E. & Schmincke, H.-U. (2004). Phase equilibria of the Lower Laacher See Tephra (East Eifel, Germany): constraints on pre-eruptive storage conditions of a phonolitic magma reservoir. *Journal of Volcanology and Geothermal Research* **134**, 135–148.

Harrison, T. M., Watson, E. B. & Aikman, A. B. (2007). Temperature spectra of zircon crystallization in plutonic rocks. *Geology* **35**, 635–638.

Hawkesworth, C., George, R., Turner, S. & Zellmer, G. (2004). Time scales of magmatic processes. *Earth and Planetary Science Letters* **218**, 1–16.

Hawkesworth, C. J., Blake, S., Evans, P., Hughes, R., MacDonald, R., Thomas, L. E., Turner, S. P. & Zellmer, G. (2000). Time scales of crystal fractionation in magma chambers; integrating physical, isotopic and geochemical perspectives. *Journal of Petrology* **41**, 991–1006.

Holland, T. J. B. & Powell, R. (1998). An internally consistent thermodynamic data set for phases of petrological interest. *Journal of Metamorphic Geology* **16**, 309–343.

Hoskin, P. W. O. & Schaltegger, U. (2003). The composition of zircon and igneous and metamorphic petrogenesis. In: Hanchar, J. M. & Hoskin, P. W. O. (eds) *Zircon. Mineralogical Society of America, Reviews in Mineralogy and Geochemistry* **52**, 27–62.

Jaffey, A. H., Flynn, K. F., Glendeni, L. E., Bentley, W. C. & Essling, A. M. (1971). Precision measurement of half-lives and specific activities of ^{235}U and ^{238}U. *Physical Review C* **4**, 1889–1906.

Liebsch, H. (1996). Die Genese der Laacher See-Karbonatite. PhD thesis. Georg-August Universität, Göttingen,, pp. 1–111.

Lowenstern, J. B., Persing, H. M., Wooden, J. L., Lanphere, M. A., Donnelly-Nolan, J. M. & Grove, T. L. (2000). U–Th dating of single zircons from young granitoid xenoliths; new tools for understanding volcanic processes. *Earth and Planetary Science Letters* **183**, 291–302.

Lustrino, M. & Wilson, M. (2007). The circum-Mediterranean anorogenic Cenozoic igneous province. *Earth-Science Reviews* **81**, 1–65.

McDonough, W. F. & Sun, S. S. (1995). The composition of the Earth. *Chemical Geology* **120**, 223–253.

Mertes, H. & Schmincke, H.-U. (1983). Age distribution of volcanoes in the West Eifel. *Neues Jahrbuch für Geologie und Paläontologie, Abhandlungen* **166**, 260–293.

Mertes, H. & Schmincke, H.-U. (1985). Mafic lavas of the Quaternary West Eifel volcanic field, I: Major and trace elements. *Contributions to Mineralogy and Petrology* **89**, 330–345.

Monteleone, B. D., Baldwin, S. L., Webb, L. E., Fitzgerald, P. G., Grove, M. & Schmitt, A. K. (2007). Late Miocene–Pliocene eclogite facies metamorphism, D'Entrecasteaux Islands, SE Papua New Guinea. *Journal of Metamorphic Geology* **25**, 245–265.

Morgan, D. J. & Blake, S. (2006). Magmatic residence times of zoned phenocrysts: introduction and application of the binary element diffusion modelling (BEDM) technique. *Contributions to Mineralogy and Petrology* **151**, 58–70.

Morgan, D. J., Blake, S., Rogers, N. W., DeVivo, B., Rolandi, G., Macdonald, R. & Hawkesworth, C. J. (2004). Time scales of crystal residence and magma chamber volume from modelling of diffusion profiles in phenocrysts: Vesuvius 1944. *Earth and Planetary Science Letters* **222**, 933–946.

Paces, J. B. & Miller, J. D., Jr (1993). Precise U–Pb ages of Duluth Complex and related mafic intrusions, northeastern Minnesota; geochronological insights to physical, petrogenetic, paleomagnetic, and tectonomagnetic processes associated with the 1·1 Ga Midcontinent Rift System. *Journal of Geophysical Research, B, Solid Earth and Planets* **98**, 13997–14013.

Park, C. & Schmincke, H.-U. (2009). Apokalypse im Rheintal. *Spektrum der Wissenschaft* **2009**, 78–87.

Pearce, N. J. G., Perkins, W. T., Westgate, J. A., Gorton, M. P., Jackson, S. E., Neal, C. R. & Chenery, S. P. (1995). A compilation of new and published major and trace element data for NIST SRM 610 and NIST SRM 612 glass reference materials. *Geostandards Newsletter* **21**, 115–144.

Pietruszka, A. J. & Garcia, M. O. (1999). The size and shape of Kilauea Volcano's summit magma storage reservoir: a geochemical probe. *Earth and Planetary Science Letters* **167**, 311–320.

Pritchard, M. E. & Simons, M. (2002). A satellite geodetic survey of large-scale deformation of volcanic centres in the central Andes. *Nature* **418**, 167–171.

Pyle, D. M., Dawson, J. B. & Ivanovich, M. (1991). Short-lived decay series disequilibria in the natrocarbonatite lavas of Oldoinyo Lengai, Tanzania: constraints on the timing of magma genesis. *Earth and Planetary Science Letters* **105**, 378–396.

Reid, M. R., Coath, C. D., Harrison, T. M. & McKeegan, K. D. (1997). Prolonged residence times for the youngest rhyolites associated with Long Valley Caldera; ^{230}Th–^{238}U ion microprobe dating of young zircons. *Earth and Planetary Science Letters* **150**, 27–39.

Riede, F. (2008). The Laacher See-eruption (12,920 BP) and material culture change at the end of the Allerod in northern Europe. *Journal of Archaeological Science* **35**, 591–599.

Scheibner, B., Heumann, A., Wörner, G. & Civetta, L. (2008). Crustal residence times of explosive phonolite magmas: U–Th ages of magmatic Ca-Garnets of Mt. Somma–Vesuvius (Italy). *Earth and Planetary Science Letters* **276**, 293–301.

Schmincke, H.-U. (2007). The Quaternary volcanic fields of the east and west Eifel (Germany). In: Ritter, J. R. R. & Christensen, U. R. (eds) *Mantle Plumes; a Multidisciplinary Approach*. Berlin: Springer, pp. 241–322.

Schmincke, H.-U. (2008). Quaternary volcanism of the east and west Eifel (Central Europe). In: McCann, T. (ed.) *Geology of Central Europe*. London: Geological Society, pp. 1318–1333.

Schmincke, H.-U., Park, C. & Harms, E. (1999). Evolution and environmental impacts of the eruption of Laacher See Volcano (Germany) 12,900 a BP. *Quaternary International* **61**, 61–72.

Schmitt, A. K. (2006). Laacher See revisited: High-spatial-resolution zircon dating indicates rapid formation of a zoned magma chamber. *Geology* **34**, 597–600.

Schuster, E. (1920). Calcitführende Auswürflinge aus dem Laacher Seegebiet. *Neues Jahrbuch für Mineralogie* **4**, 295–318.

Sims, K. W. W., Gill, J. B., Dosseto, A., Hoffmann, D. L., Lundstrom, C. C., Williams, R. W., Ball, L., Tollstrup, D., Turner, S., Prytulak, J., Glessner, J. J. G., Standish, J. J. & Elliott, T. (2008). An inter-laboratory assessment of the thorium isotopic composition of synthetic and rock reference materials. *Geostandards and Geoanalytical Research* **32**, 65–91.

Spell, T. L., Smith, E. I., Sanford, A. & Zanetti, K. A. (2001). Systematics of xenocrystic contamination: preservation of discrete feldspar populations at McCullough Pass Caldera revealed by ^{40}Ar/^{39}Ar dating. *Earth and Planetary Science Letters* **190**, 153–165.

Streckeisen, A. (1979). Classification of volcanic rocks, lamprophyres, carbonatites, and melilitic rocks—recommendations and suggestions of the IUGS Subcommission on the Systematics of Igneous Rocks—reply. *Geology* **7**, 562–562.

Tait, S. R., Wörner, G., Bogaard, v. d. P. & Schmincke, H.-U. (1989). Cumulate nodules as evidence for convective fractionation in a phonolite magma chamber. *Journal of Volcanology and Geothermal Research* **37**, 21–37.

Taylor, H. P., Frechen, J. & Degens, E. T. (1967). Oxygen and carbon isotope studies of carbonatites from Laacher See District, West Germany, and Alno District, Sweden. *Geochimica et Cosmochimica Acta* **31**, 407–430.

Trail, D., Mojzsis, S. J., Harrison, T. M., Schmitt, A. K., Watson, E. B. & Young, E. D. (2007). Constraints on Hadean zircon protoliths from oxygen isotopes, Ti-thermometry, and rare earth elements. *Geochemistry, Geophysics, Geosystems* **8**, doi:10.1029/2006GC001449.

Trail, D., Bindeman, I. N., Watson, E. B. & Schmitt, A. K. (2009). Experimental calibration of oxygen isotope fractionation between quartz and zircon. *Geochimica et Cosmochimica Acta* **73**, 7110–7126.

Valley, J. W. (2003). Oxygen isotopes in zircon. In: Hanchar, J. M. & Hoskin, P. W. O. (eds) *Zircon. Mineralogical Society of America, Reviews in Mineralogy and Geochemistry* **52**, 343–385.

Watson, E. B. (1979). Zircon saturation in felsic liquids: experimental results and applications to trace element geochemistry. *Contributions to Mineralogy and Petrology* **70**, 407–419.

Watson, E. B. & Harrison, T. M. (1983). Zircon saturation revisited: temperature and composition effects in a variety of crustal magma types. *Earth and Planetary Science Letters* **64**, 295–304.

Wicks, C. W., Dzurisin, D., Ingebritsen, S., Thatcher, W., Lu, Z. & Iverson, J. (2002). Magmatic activity beneath the quiescent Three Sisters volcanic center, central Oregon Cascade Range, USA. *Geophysical Research Letters* **29**, doi:10.1029/2001GL014205.

Wiedenbeck, M., Hanchar, J. M., Peck, W. H. *et al.* (2004). Further characterisation of the 91500 zircon crystal. *Geostandards and Geoanalytical Research* **28**, 9–39.

Williams, R. W., Gill, J. B. & Bruland, K. W. (1986). Ra–Th disequilibria systematics—timescale of carbonatite magma formation at Oldoinyo-Lengai Volcano, Tanzania. *Geochimica et Cosmochimica Acta* **50**, 1249–1259.

Wilson, M. & Downes, H. (1991). Tertiary–Quaternary extension-related alkaline magmatism in western and central Europe. *Journal of Petrology* **32**, 811–849.

Woolley, A. R. & Kjarsgaard, B. A. (2008). *Carbonatite occurrences of the world; map and database. Geological Survey of Canada, Open File Report* **5796.**

Wörner, G. & Schmincke, H.-U. (1984*a*). Mineralogical and chemical zonation of the Laacher See tephra sequence (East Eifel, W. Germany). *Journal of Petrology* **25**, 805–835.

Wörner, G. & Schmincke, H.-U. (1984*b*). Petrogenesis of the zoned Laacher See Tephra. *Journal of Petrology* **25**, 836–851.

Wörner, G. & Wright, T. L. (1984). Evidence for magma mixing within the Laacher See magma chamber (East Eifel, Germany). *Journal of Volcanology and Geothermal Research* **22**, 301–327.

Wörner, G., Beusen, J. M., Duchateau, N., Gijbels, R. & Schmincke, H.-U. (1983). Trace element abundances and mineral/melt distribution coefficients in phonolites from the Laacher See Volcano (Germany). *Contributions to Mineralogy and Petrology* **84**, 152–173.

Wörner, G., Staudigel, H. & Zindler, A. (1985). Isotopic constraints on open system evolution of the Laacher See magma chamber (Eifel, West Germany). *Earth and Planetary Science Letters* **75**, 37–49.

Wörner, G., Harmon, R. & Hoefs, J. (1987). Stable isotope relationships in an open magma system, Laacher See, Eifel (F.R.G.). *Contributions to Mineralogy and Petrology* **95**, 343–349.

Wörner, G., Viereck, L., Plaumann, S., Pucher, R., Bogaard, v. d. P. & Schmincke, H.-U. (1988). The Quaternary Wehr Volcano—a multiphase evolved eruption center in the East Eifel Volcanic Field (FRG). *Neues Jahrbuch für Mineralogie, Abhandlungen* **159**, 73–99.

Zellmer, G. F., Blake, S., Vance, D., Hawkesworth, C. & Turner, S. (1999). Plagioclase residence times at two island arc volcanoes (Kameni Islands, Santorini, and Soufrière, St. Vincent) determined by Sr diffusion systematics. *Contributions to Mineralogy and Petrology* **136**, 345–357.